

Approaches for Road Surface Roughness Estimation Using Airborne Polarimetric SAR

Arun Babu , Graduate Student Member, IEEE, Stefan V. Baumgartner , Senior Member, IEEE, and Gerhard Krieger , Fellow, IEEE

Abstract—The road surface roughness is an important parameter that determines the quality of a road network. It has a direct influence on the grip and skid resistance of the vehicles. For this reason, this parameter has to be periodically monitored to keep track of its changes. Nowadays, road surface roughness is measured by driving measurement vehicles equipped with laser scanners all over the country. But, this approach is very costly, labor-intensive, and time-consuming. This article is done to evaluate the potential of high-resolution airborne polarimetric synthetic aperture radar (SAR) to remotely estimate the road surface roughness on a wide scale. Different SAR backscatter-based semi-empirical models and SAR polarimetry-based models for surface roughness estimation are implemented in this article. Also, a new semi-empirical model is proposed in this article, which is trained specifically for the road surface roughness estimation. Additive noise subtraction, upper sigma nought threshold masking, and lower signal-to-noise ratio threshold masking techniques were implemented in this article to improve the reliability of road surface roughness estimation. The feasibility of this approach is tested using fully polarimetric X-band datasets acquired with DLR’s airborne radar sensor F-SAR. The surface roughness results estimated using these airborne SAR datasets show good agreement with the ground truth surface roughness values and the results are discussed in this article.

Index Terms—Additive noise, anisotropy, coherency matrix, Dubois model, Oh model, open street map (OSM), road surface roughness, synthetic aperture radar (SAR).

I. INTRODUCTION

THE road infrastructure has a major role in the economic growth and development of a country. The quality of the road network directly influences the safety, health, driving comfort, and seamless transport of goods and services [1]–[3]. Therefore, periodic monitoring and maintenance of the road infrastructure quality is a necessity. The road surface roughness is one of the important factors which affect the road surface quality [4]–[6].

The road surface roughness is responsible for the friction between the road and the tires of the vehicles [7], [8]. So it affects the “grip” or “skid resistance” of the vehicle [9], [10]. Fig. 1(a) shows an example of the vertical road surface profile.

Manuscript received October 27, 2021; revised March 25, 2022; accepted April 8, 2022. Date of publication April 26, 2022; date of current version May 11, 2022. This work was supported by the German Academic Exchange Service under Grant 57478193. (Corresponding author: Arun Babu.)

The authors are with the Radar Concepts Department, Microwaves and Radar Institute, German Aerospace Center, 82234 Oberpfaffenhofen, Germany (e-mail: arun.babu@dlr.de; stefan.baumgartner@dlr.de; gerhard.krieger@dlr.de).

Digital Object Identifier 10.1109/JSTARS.2022.3170073

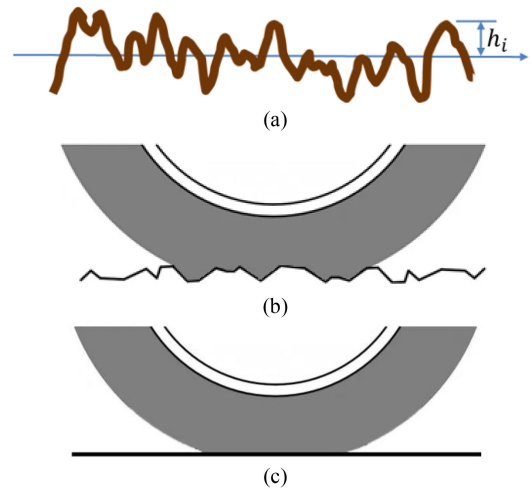


Fig. 1. Road surface roughness visualization. (a) Vertical road surface profile. (b) Contact between a rough road surface and tire (road vertical profile is exaggerated for better visualization). (c) Contact between a very smooth road surface and tire.

This undulated vertical profile of the road provides sufficient friction between the road surface and the tires [11]. The Root Mean Square (rms) height (h_{rms}) of the vertical profile can be considered as a measure of the road surface roughness and it can be estimated as follows [12], [13]:

$$h_{rms} = \sqrt{\frac{\sum_{i=1}^n (h_i - \bar{h})^2}{n-1}} \quad (1)$$

where h_i is the vertical height at location i and \bar{h} represents the mean vertical height of the surface for n samples.

Fig. 1(b) shows the contact between a rough road surface and tire. In this case, due to the weight acting up on the tire and also due to the vertical profile of the road, the vertical rough points on the road penetrates the tire rubber. Because of the tire rubber’s flexibility, the rubber adapts to the shape of rough points on the road surface and in turn, increases the contact surface area between the road surface and the tire [14]. This behavior results in a better “grip” and the chances of tire skid are less [15]. Fig. 1(c) shows the contact between a very smooth road surface and tire. In this case, there are no sufficient vertical rough points on the road surface and the contact surface area between the road surface and the tire is less compared to Fig. 1(b). Therefore,

less friction is offered in this case and the chances of skid are more [14], [15]. From Fig. 1(b) and (c), it can be said that an optimum amount of skid resistance is required for performing safe acceleration, deceleration, and steering maneuvers. But, too high surface roughness can also affect the driving comfort, fuel consumption, and also leads to high noise [16].

All the abovementioned factors point out the requirement of periodic monitoring of the road surface quality to ensure that the friction provided by the road surface is in the optimum range. The friction depends on the road surface roughness and the material used for road surface construction. So the road surface roughness can be considered as a measure of the friction. But, nowadays, road surface friction is measured using measurement vehicles. This measurement process requires enormous costs for the entire road network because of its labor-intensive and time-consuming nature [17].

This article focuses on evaluating the potential of airborne polarimetric synthetic aperture radar (SAR) to remotely estimate the road surface conditions on a large scale. So far, only a few publications are available for road surface roughness estimation using SAR [18], [19]. The main objective of this article is to investigate and develop efficient and reliable methods for road surface roughness estimation using high-resolution airborne polarimetric SAR (PolSAR) over a wide region.

II. TEST SITE DESCRIPTION

Road networks with different surface roughness values are required for this article. For this purpose, three different test sites were identified. The first test site is the Kaufbeuren airfield in Bavaria, Germany. It is a former military airfield that includes the runway, taxiways, and parking area composed of different materials like asphalt, concrete, etc. The Google Earth image of the Kaufbeuren test site is shown in Fig. 2(a). The zoomed view on the top left side of the image shows the concrete and asphalt sections on the runway. The zoomed view on the bottom right side of the image shows the parking area with cracks and potholes. The repair works done on the runway are also visible in the zoomed view.

The second site is the “Demonstrations-, Untersuchungs- und Referenzareal der BASt (duraBASt)” test site in Cologne, Germany. It is located near the motorway intersection Cologne-East and is maintained by the Federal Highway Research Institute of Germany known as “Bundesanstalt für Straßenwesen” [20]. Fig. 2(b) shows the Google Earth image of the Cologne motorway intersection and the zoomed view shows the duraBASt test site. The duraBASt test site is the area inside the yellow ellipse parallel to the motorway shown in the zoomed view. From Fig. 2(b), it can be seen that the regions of the duraBASt test site are appearing in different colors and this is due to the different materials used for its construction. These different materials are having different surface roughness values and this makes this site suitable for this article.

The third test site is the Wolfsburg motorway intersection at Braunschweig, Germany. This test site is selected because of the long motorway without any disturbance from trees, buildings,

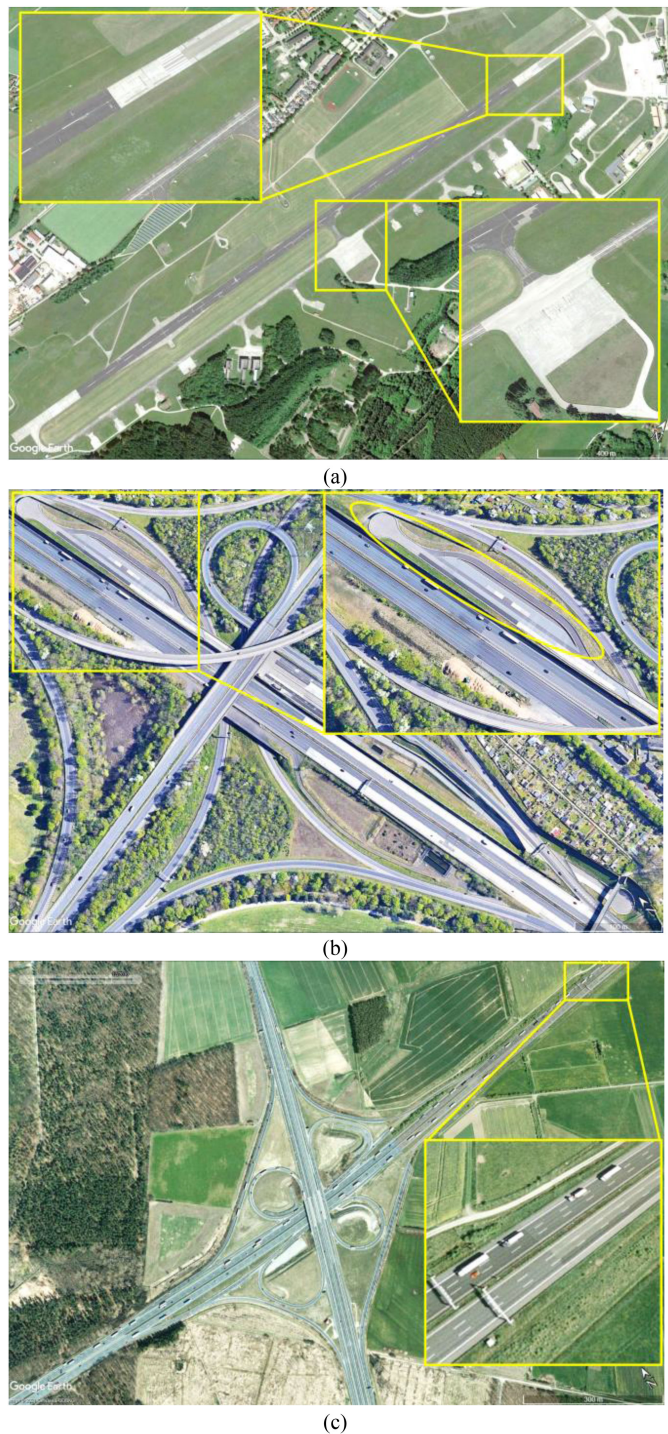


Fig. 2. Test sites used for this article. (a) Kaufbeuren test site, Bavaria. (b) DuraBASt test site, Cologne. (c) Wolfsburg motorway intersection, Braunschweig.

etc. Fig. 2(c) shows the Google Earth image of this test site. Uniform surface roughness is expected at this test site. Toward the top right end of the image, it can be seen that there is a sudden change in the color shade of the motorway. This may be due to repair work done at that region and a change in surface roughness can be expected there.

TABLE I
GENERAL CHARACTERISTICS OF THE F-SAR DATASETS

SAR system	F-SAR
Frequency band	X-band (9.60 GHz)
Polarimetric mode	Quad-pol
Look direction	Right
Spatial resolution	25 cm x 25 cm

III. DATASET DESCRIPTION

The details about the airborne SAR datasets and the ground truth (GT) data used for this article are explained in this section.

A. F-SAR Datasets

Fully polarimetric X-band airborne SAR datasets acquired by DLR's F-SAR system are used for this article [21], [22]. The F-SAR system is mounted on a Dornier DO228-212 aircraft and it is flown over the Kaufbeuren, Cologne, and Braunschweig test sites described in the previous section. The general characteristics of the F-SAR datasets used in this article are given in Table I.

The datasets were acquired over the Cologne test site on 10th September 2019, over the Braunschweig test site on 31st August 2020, and finally over the Kaufbeuren test site on 4th September 2020. At each test site, several datasets were acquired from different directions (i.e., with different aspect angles) and also with different incidence angles.

B. Ground Truth Data Collection

A ground truth (GT) data collection activity has been performed at the Kaufbeuren test site on 3rd September 2020 to measure the GT surface roughness values ($GT h_{rms}$). The GT data collection activity was performed just 1 day before the airborne SAR data acquisition to avoid any unexpected changes between the airborne SAR datasets and the GT data. The GT data were also acquired on a dry sunny day to prevent any measurement errors caused due to water filling the voids in concrete and asphalt surfaces.

Ten GT spots with each of 1 m² area were identified for the GT data collection. Fig. 3 shows the location of these GT spots in the Google Earth image and also the photos of the GT spots. From Fig. 3, it can be seen that the GT spots were distributed over the runway, taxiway, and parking areas covering both smooth and rough regions made of concrete and asphalt.

The $GT h_{rms}$ values were measured by laser scanning using a handheld laser scanner. The handheld laser scanner used for this purpose measured the vertical surface undulations of the road surface with a measurement resolution of 0.025 mm and also with an accuracy of 0.025 mm.

Fig. 4(a) shows the $GT h_{rms}$ measurement process using the handheld laser scanner. Fig. 4(b) shows the surface undulations image generated from the laser scanner data for GT spot 1. A single $GT h_{rms}$ value was then calculated for each of the GT spots from the surface undulation values using (1).

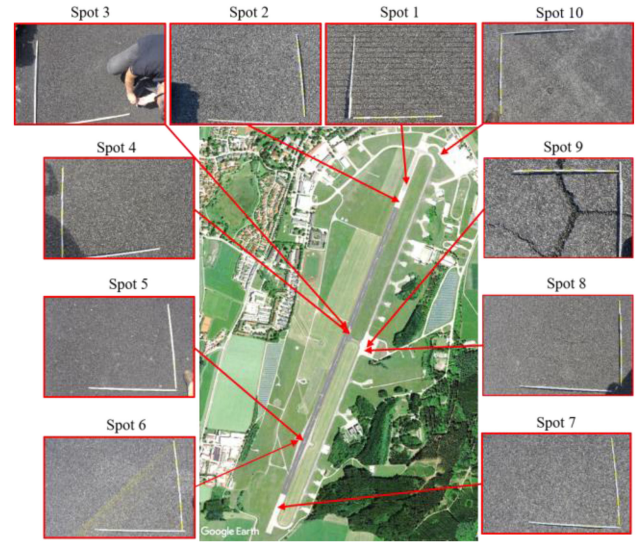


Fig. 3. Ground truth spots at Kaufbeuren test site.

TABLE II
GROUND TRUTH SURFACE ROUGHNESS DATA

GT spot	Surface undulation (mm)		$GT h_{rms}$ (mm)	Remarks
	Min	Max		
1	-7.09	2.73	2.36	Repeated directional grooves
2	-3.00	2.27	0.99	Concrete, smooth
3	-2.53	1.70	0.66	Asphalt, smooth
4	-4.34	1.66	0.88	Maintenance work, smooth
5	-2.45	2.26	0.68	Asphalt, smooth
6	-4.14	2.01	0.98	Concrete, smooth
7	-3.03	2.62	1.09	Concrete, smooth
8	-2.38	1.91	0.61	Concrete, very smooth
9	-	4.25	2.86	Deep, non-oriented cracks
10	-5.82	1.92	0.76	Concrete, very smooth

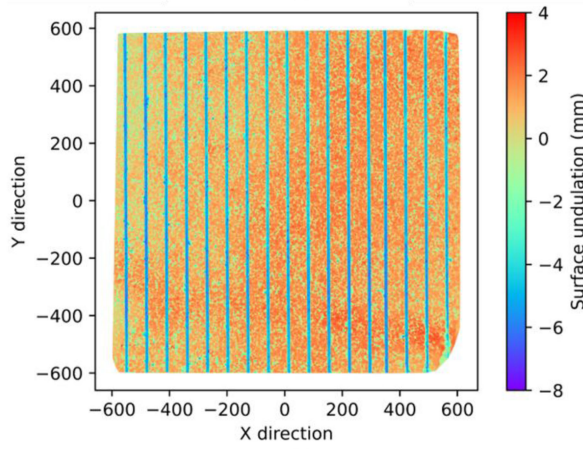
Table II shows the maximum–minimum surface undulations and $GT h_{rms}$ values estimated for each of the GT spots. These $GT h_{rms}$ values can be used to validate the surface roughness values estimated from the polarimetric airborne SAR datasets.

IV. METHODOLOGY

As discussed in the introduction section, the rms height (h_{rms}) can be considered as a measure of the road surface roughness (1). So the h_{rms} needs to be estimated from the PolSAR data. Several studies were done in the past to estimate the soil surface roughness and soil moisture using PolSAR datasets [23]–[25]. In these articles, the remotely sensed parameter (ks) was derived which represents the effective vertical roughness and it is a unitless parameter [12], [13]. The surface roughness (h_{rms}) can



(a)



(b)

Fig. 4. Ground truth data collection at Kaufbeuren test site. (a) GT h_{rms} measurement process. (b) Surface undulations image.

be estimated from the (ks) as follows:

$$h_{\text{rms}} = \frac{ks}{(2\pi/\lambda_c)} \quad (2)$$

where λ_c is the wavelength corresponding to the center frequency of the SAR system.

In this article also, the effective vertical surface roughness (ks) parameter was estimated to derive the road surface roughness (h_{rms}). This section explains the methodology adopted in this article for estimating the effective vertical surface roughness (ks) parameter. The process flowchart is shown in Fig. 5.

Since the SAR backscatter received from the road surfaces is very low, the multiplicative noise and additive noise present in the airborne PolSAR data needs to be minimized for the reliable estimation of the road surface roughness.

Speckle is the dominant multiplicative noise present in the SAR data [26]. It appears as a granular disturbance and occurs due to the coherent imaging of the SAR systems. For this article, the speckle present in the PolSAR data was minimized by speckle filtering using a Refined-Lee speckle filter with a 3×3 window [27].

The additive noise present in the PolSAR data is caused by the thermal/system noise of the SAR system [28]. In addition to the speckle filtering, the additive noise present in the PolSAR data needs to be minimized for low signal-to-noise ratio (SNR)

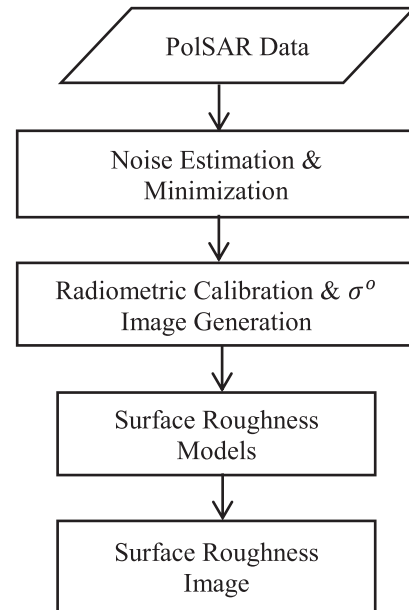


Fig. 5. Process flowchart for surface roughness estimation.

applications [29]. The additive noise estimation algorithm used in this article requires the PolSAR data in the 4×4 coherency matrix (T_4) form. Therefore, the T_4 matrix was generated from the speckle filtered dataset [12]. The additive noise estimation and minimization procedure were then carried out on T_4 and thereafter the noise minimized dataset was used for generating the radiometrically calibrated sigma nought images. The sigma nought images were then used as the input for the surface roughness estimation models to generate the surface roughness images.

A. Noise Estimation and Minimization

The PolSAR is an advanced imaging radar system that uses the different polarization states of an electromagnetic wave of the same center frequency to analyze the scattering information from different ground targets. From a fully PolSAR system, four polarimetric channels can be obtained: horizontal polarization transmitted and horizontal (S_{HH}) and vertical polarization (S_{HV}) received simultaneously; vertical polarization transmitted and horizontal (S_{VH}) and vertical polarization (S_{VV}) received simultaneously. But, the PolSAR datasets are commonly affected by the additive noise present in each of the polarimetric channels [28]. This additive noise present in the dataset adversely affects the accurate estimation of the useful parameters from the polarimetric data [29], [30]. So the additive noise present in the PolSAR data must be filtered out before using the dataset for any quantitative analysis like the road surface roughness estimation. The procedure for additive noise removal is described in this section. The information obtained from the four polarimetric channels can be represented in the form of the measured scattering matrix [S'], ideal scattering matrix free from additive noise [S], and additive noise matrix [N] as follows [28]:

$$[S'] = [S] + [N] \quad (3)$$

where

$$[S] = \begin{bmatrix} S_{HH} & S_{HV} \\ S_{VH} & S_{VV} \end{bmatrix} \text{ and } [N] = \begin{bmatrix} n_{HH} & n_{HV} \\ n_{VH} & n_{VV} \end{bmatrix}.$$

The additive noise present in the data can be considered as a zero-mean Gaussian white noise process and the additive noise power N can be modeled as [28]

$$\langle n_{ij}n_{ij}^* \rangle = \langle n_{mn}n_{mn}^* \rangle = N \text{ and } \langle n_{ij}n_{mn}^* \rangle = 0 \quad (4)$$

where $*$ is the complex conjugate operator.

The Pauli basis vector corresponding to the measured scattering matrix $[S']$ can be written as [28]

$$k_{3p} = \frac{1}{\sqrt{2}} \begin{bmatrix} S_{HH} + S_{VV} + (n_{HH} + n_{VV}) \\ S_{HH} - S_{VV} + (n_{HH} - n_{VV}) \\ S_{HV} + S_{VH} + (n_{HV} - n_{VH}) \end{bmatrix}. \quad (5)$$

The noise affected 3×3 coherency matrix corresponding to the measured scattering matrix $[S']$ can be estimated by the spatial averaged multiplication of the Pauli basis vector with the transpose of its complex conjugate as follows [28]:

$$[T_{3 \text{ noise affected}}] = \langle k_{3p} \cdot k_{3p}^{*T} \rangle = \frac{1}{2} \times \begin{bmatrix} T_{11} + 2N & T_{12} & T_{13} \\ T_{21} & T_{22} + 2N & T_{23} \\ T_{31} & T_{32} & T_{33} + 2N \end{bmatrix}. \quad (6)$$

For a monostatic SAR system, the cross-polarized channels are completely correlated in the absence of additive noise ($S_{HV} = S_{VH}$) [28]. This is because a monostatic SAR follows the scattering reciprocity condition. Since the two cross-polarized channels are measured independently by the SAR system, the additive noise level present in the two cross-polarized channels will be different. So as the additive noise level increases, the correlation between the cross-polarized channels decreases. This decorrelation between the cross-polarization channels can be utilized to estimate the additive noise power N . Since the scattering reciprocity condition is not valid for noisy data, the 4-D Pauli basis vector is required and it can be written as follows [28]:

$$k_{4p} = \frac{1}{\sqrt{2}} \begin{bmatrix} S_{HH} + S_{VV} + (n_{HH} + n_{VV}) \\ S_{HH} - S_{VV} + (n_{HH} - n_{VV}) \\ S_{HV} + S_{VH} + (n_{HV} - n_{VH}) \\ i(S_{HV} - S_{VH} + (n_{HV} - n_{VH})) \end{bmatrix}. \quad (7)$$

This k_{4p} vector can be used to estimate the noise affected 4×4 coherency matrix as [28]

$$[T_{4 \text{ noise affected}}] = \langle k_{4p} \cdot k_{4p}^{*T} \rangle. \quad (8)$$

The diagonalization of the 4×4 coherency matrix ($[T_{4 \text{ noise affected}}]$) leads to the following form [28]:

$$[\Lambda_4] = [U_4] [T_{4 \text{ noise affected}}] [U_4]^{-1} = \begin{bmatrix} \lambda_1 + N & 0 & 0 & 0 \\ 0 & \lambda_2 + N & 0 & 0 \\ 0 & 0 & \lambda_3 + N & 0 \\ 0 & 0 & 0 & N \end{bmatrix} \quad (9)$$

where λ_1 , λ_2 , and λ_3 are the first three eigenvalues of the 4×4 coherency matrix and N is the additive noise present in the data.

In the absence of noise, the 4×4 coherency matrix has a rank of 3, and only the first three eigenvalues λ_1 , λ_2 , and λ_3 have nonzero values. But, the presence of noise makes the 4×4 coherency matrix be of rank 4 and the fourth eigenvalue λ_4 represents the additive noise present in the data ($\lambda_4 = N$). So the additive noise can be filtered out by subtracting the additive noise power N from the first three eigenvalues of the coherency matrix or by subtracting N from the diagonal elements of the $[T_{3 \text{ noise affected}}]$ as follows [28]:

$$[T_3] = [T_{3 \text{ noise affected}}] - N \begin{bmatrix} 1 & 0 & 0 \\ 0 & 1 & 0 \\ 0 & 0 & 1 \end{bmatrix} \quad (10)$$

where $[T_3]$ is the noise filtered 3×3 coherency matrix.

From the noise filtered 3×3 coherency matrix $[T_3]$, the scattering matrix elements can be estimated as

$$|S_{HH}|^2 = \frac{(T_{11} + 2 * Re\{T_{12}\} + T_{22})}{2}, |S_{HV}|^2 = \frac{T_{33}}{2} |S_{VV}|^2 = \frac{(T_{11} - 2 * Re\{T_{12}\} + T_{22})}{2}. \quad (11)$$

The radiometrically calibrated sigma nought (σ^o) images can be generated as [22]

$$\sigma_{HH}^o = \sin \theta * |S_{HH}|^2, \sigma_{HV}^o = \sin \theta * |S_{HV}|^2, \sigma_{VV}^o = \sin \theta * |S_{VV}|^2 \quad (12)$$

where θ is the local incidence angle.

B. Description of the SAR Polarimetry-Based Models

This subsection describes the SAR polarimetry-based models implemented in this article for estimating the effective vertical surface roughness parameter (ks). The SAR polarimetry-based models utilize both the amplitude and phase information of the copolarization and cross-polarization channels for the ks estimation. The anisotropy-based model and coherency matrix-based model were implemented in this article. The description of these models is given as follows.

1) *Anisotropy-Based Model*: In the anisotropy-based model, the polarimetric anisotropy parameter (A) is utilized to estimate ks [12]. The anisotropy parameter is derived from the minor eigenvalues of the additive noise removed 3×3 coherency matrix as follows [31], [32]:

$$A = \frac{\lambda_2 - \lambda_3}{\lambda_2 + \lambda_3} \quad (13)$$

where λ_2 and λ_3 are the second and third largest eigenvalues of the coherency matrix.

The effective vertical surface roughness (ks) can be estimated as follows [12], [13]:

$$ks = 1 - A. \quad (14)$$

2) *Coherency Matrix-Based Model*: In the coherency matrix-based model, the T_{22} and T_{33} elements of the additive

noise removed coherency matrix is used to estimate the effective vertical surface roughness (ks) [12], [13]

$$ks = 1 - \frac{T_{22} - T_{33}}{T_{22} + T_{33}}. \quad (15)$$

C. Description of the Semi-Empirical Models

This subsection describes the semi-empirical models used in this article for estimating the effective vertical surface roughness (ks). In contrast to the SAR polarimetry-based models, the semi-empirical models require only the SAR backscatter values (σ^o) instead of the amplitude and phase information. The Oh models and the Dubois model were implemented in this article.

1) *Oh Models*: The Oh models developed in 1992 and 2004 were originally developed for soil roughness and soil moisture estimation. In the Oh 1992 model, the Fresnel reflectivity (Γ^o) is estimated to derive the ks . Γ^o is estimated by solving the nonlinear equation given as follows using an iterative root-finding algorithm [33]:

$$\left(\frac{2\theta}{\pi}\right)^{\frac{1}{\Gamma^o}} \left[1 - \frac{q}{0.23\sqrt{\Gamma^o}}\right] + \sqrt{p} - 1 = 0. \quad (16)$$

After estimating Γ^o , ks can be estimated as follows [33]:

$$ks = \ln \left(\frac{(\sqrt{p} + 1)}{\left(\frac{2\theta}{\pi}\right)^{\frac{1}{\Gamma^o}}} \right) \quad (17)$$

where θ is the local incidence angle, p is the copolarization ratio given by $p = \frac{\sigma_{HH}^o}{\sigma_{VV}^o}$, and q is the cross-polarization ratio given by $q = \frac{\sigma_{HV}^o}{\sigma_{VH}^o}$, and σ_{HH}^o and σ_{VV}^o are the copolar sigma nought values for HH and VV polarization channels, respectively.

In the Oh 2004 model, the surface moisture mv is estimated instead of the Fresnel reflectivity Γ^o to derive the ks . Similar to the estimation of Γ^o , mv is also estimated by solving the nonlinear equation using an iterative root-finding algorithm [34]

$$1 - \left(\frac{\theta}{90}\right)^{0.35mv^{-0.65}} e^{-0.65} \times \left[\left[-3.125 \ln \left\{ 1 - \frac{\sigma_{VH}^o}{0.11mv^{0.7} \cos^{2.2}\theta} \right\} \right]^{0.556} \right]^{1.4} - p = 0. \quad (18)$$

After estimating mv , ks can be estimated as follows [34]:

$$ks = \left[-3.125 \ln \left\{ 1 - \frac{\sigma_{VH}^o}{0.11mv^{0.7} \cos^{2.2}\theta} \right\} \right]^{0.556} \quad (19)$$

where θ is the local incidence angle.

The ks values estimated from both Oh models have a validity range of $0.1 < ks < 6.0$. The ks values outside this validity range should be discarded. For the X-band SAR used in this article with 9.60 GHz center frequency, this corresponds to an h_{rms} validity range of $0.14 \text{ mm} < h_{rms} < 8.17 \text{ mm}$.

2) *Dubois Model*: The Dubois model developed in 1995 is a semi-empirical model developed for soil roughness and soil moisture estimation. The inversion of ks using the Dubois model

is a two-step noniterative process. The first step is to estimate the dielectric constant (ϵ') as follows [35]:

$$\epsilon' = \frac{\left(\log_{10} \left(\frac{(\sigma_{HH}^o)^{0.7857}}{\sigma_{VV}^o} \right) \right) 10^{-0.19} \cos^{1.82}\theta \sin^{0.93}\theta \lambda^{0.15}}{-0.024 \tan \theta} \quad (20)$$

where σ_{HH}^o and σ_{VV}^o are the copolar sigma nought values for the HH and VV channels, respectively.

The second step is to derive the ks from the estimated dielectric constant (ϵ') as [35]

$$ks = \sigma_{HH}^o / 1.410^{2.75/1.4} \frac{\sin^{2.57}\theta}{\cos^{1.07}\theta} 10^{-0.02\epsilon' \tan \theta} \lambda^{-0.5} \quad (21)$$

where θ is the local incidence angle and λ is the wavelength of the radar.

The ks values estimated using the Dubois model are valid only when $ks < 2.5$ and $\theta > 30^\circ$. The ks values that do not satisfy both conditions should be discarded. For the X-band SAR used in this article with 9.60 GHz center frequency, this corresponds to an h_{rms} validity range of $h_{rms} < 12.43 \text{ mm}$.

D. Development of a New Semi-Empirical Model

This subsection explains the development of a new semi-empirical model suitable for reliable road surface roughness estimation. The new model was developed based on the Dubois model. According to the assumptions from the Dubois model, a radar signal in pq polarization can be written as a function of incidence angle, surface roughness, and surface moisture [36]. But, for a dry asphalt or concrete surface, the contribution from the surface moisture component to the radar signal is negligible. So for the new model formulation, the radar signal can be written as a function of incidence angle and surface roughness after neglecting the surface moisture component. The relationship can be written as follows [37]:

$$\sigma_{pq}^o = \delta (\cos(\theta))^\beta (ks)^\epsilon \sin(\theta). \quad (22)$$

In the above equation, σ_{pq}^o is the sigma nought backscatter value for the p transmitted and q received polarization. The term $\delta (\cos(\theta))^\beta$ denotes the relationship between σ_{pq}^o and the local incidence angle (θ). From this relationship, it can be understood that the σ_{pq}^o decreases as the incidence angle (θ) increases and this decrease in σ_{pq}^o is higher at low incidence angles and lower at high incidence angles [37]–[39].

The second term $(ks)^\epsilon \sin(\theta)$ indicates the relationship between σ_{pq}^o and the effective surface roughness (ks). σ_{pq}^o and ks have a power law relationship and the sensitivity of σ_{pq}^o to ks is higher at high incidence angles than at low incidence angles [37], [40], [41]. The $\sin(\theta)$ term is added to the relationship to minimize this incidence angle dependency [37].

Equation (22) can be inverted to estimate ks as a function of σ_{pq}^o and incidence angle (θ) as follows:

$$ks = 10^{\left[\frac{\log(\sigma_{pq}^o) - \log(\delta (\cos(\theta))^\beta)}{\epsilon \sin(\theta)} \right]}. \quad (23)$$

In (23), δ , β , and ϵ are the unknown coefficients that need to be estimated to solve the equation. The coefficients can be

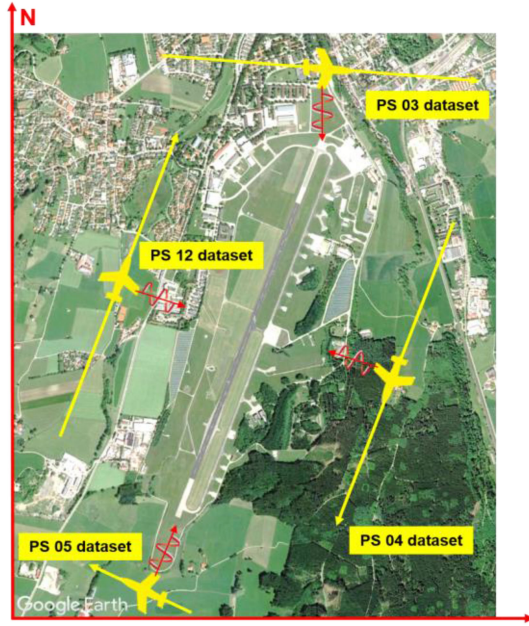


Fig. 6. Acquisition geometry of the F-SAR datasets over the Kaufbeuren test site.

TABLE III
METADATA OF TRAINING AND TESTING DATASETS

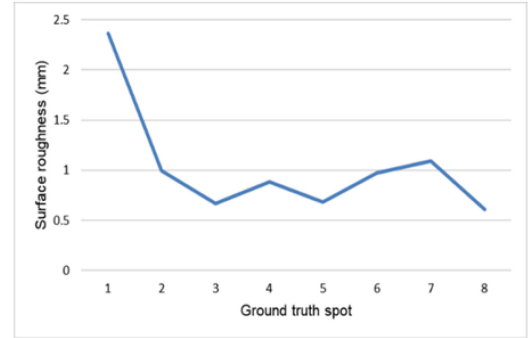
Data ID	Flight heading direction (deg)	Aspect angle (deg)	Incidence angle at the runway (deg)	Used for
PS 03	91.20	181.20	28.67 to 55.06	Testing
PS 04	201.71	291.71	28.72 to 32.09	Training
PS 05	291.68	21.68	32.04 to 55.46	Training
PS 12	21.70	111.70	38.96 to 41.89	Training

estimated using the GT h_{rms} values, σ_{pq}^o values, and incidence angle values (θ) at the GT spots using the method of least square-based curve fitting.

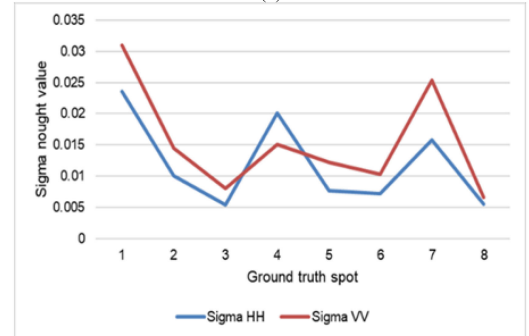
Three F-SAR datasets (PS 04 dataset, PS 05 dataset, and PS 12 dataset) acquired over the Kaufbeuren test site were taken to estimate the δ , β , and ε coefficients. The datasets were acquired from three different sides of the Kaufbeuren runway (Fig. 6). The PS 03 dataset shown in Fig. 6 was used to test the new model after coefficient estimation because it has a different acquisition geometry compared to the other three datasets used to estimate the model coefficients.

The flight heading direction, aspect angle, and incidence angle values at the runway are shown in Table III. The aspect angle is the SAR look direction toward the runway measured from the north direction. From Table III, it can be understood that the three training datasets have completely different aspect angles and incidence angles for the runway and this can help in the unbiased estimation of the model coefficients.

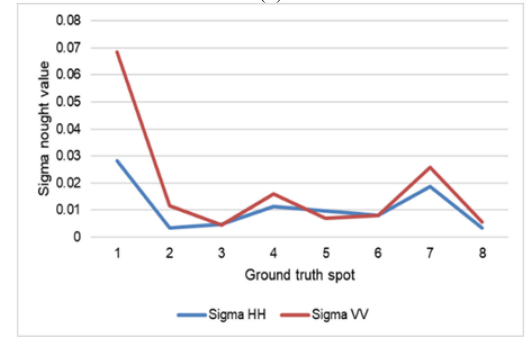
Fig. 7(a) shows the GT h_{rms} plot for the GT spots 1–8. Fig. 7(b)–(d) shows the σ_{HH}^o and σ_{VV}^o plots for the PS 04, PS 05, and PS 12 datasets, respectively. The σ_{HH}^o and σ_{VV}^o plots are shown for the GT spots 1–8. By comparing Fig. 7(a) with



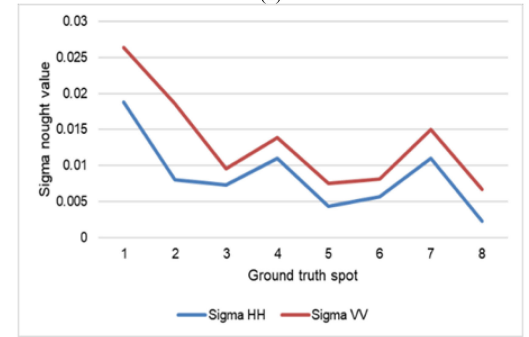
(a)



(b)



(c)



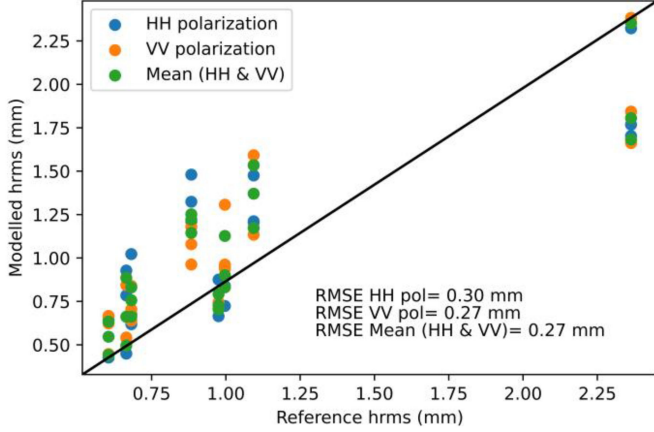
(d)

Fig. 7. Correlation between GT h_{rms} and σ^o values. (a) GT h_{rms} plot. (b) σ_{HH}^o and σ_{VV}^o plots for PS 04 dataset. (c) σ_{HH}^o and σ_{VV}^o plots for PS 05 dataset. (d) σ_{HH}^o and σ_{VV}^o plots for PS 12 dataset.

Fig. 7(b)–(d), it can be seen that the σ_{HH}^o and σ_{VV}^o plots are following the same trend as the GT h_{rms} plot. This indicates that the GT h_{rms} changes are correlated with the σ_{HH}^o and σ_{VV}^o magnitude changes. This correlation between the GT h_{rms} , σ_{HH}^o , and σ_{VV}^o was utilized to estimate the model coefficients for the new model. For this purpose, the GT h_{rms} , σ_{HH}^o , σ_{VV}^o , and

TABLE IV
 COEFFICIENTS ESTIMATED FOR THE NEW MODEL

Coefficients	Polarization	
	HH	VV
δ	0.06782502	0.06792563
β	-0.9301637	-2.46489793
ε	2.23988886	2.27478606


 Fig. 8. GT h_{rms} vs. model-estimated surface roughness.

incidence angle (θ) values of these three datasets for the GT spots 1–8 were used as inputs for the least square-based curve fitting algorithm and the model coefficients were estimated.

The model coefficients were estimated for the HH and VV polarizations separately and the values are shown in Table IV.

Using the model coefficient values from Table IV, (23) can be written as

$$k_{s_{HH}} = 10^{\left[\frac{\log(\sigma_{pq}^{\circ}) - \log(0.06782502(\cos(\theta))^{-0.9301637})}{2.23988886 \sin(\theta)} \right]}$$

$$k_{s_{VV}} = 10^{\left[\frac{\log(\sigma_{pq}^{\circ}) - \log(0.06792563(\cos(\theta))^{-2.46489793})}{2.27478606 \sin(\theta)} \right]} \quad (24)$$

where $k_{s_{HH}}$ is the ks value estimated for the HH polarization and $k_{s_{VV}}$ is the ks value estimated for the VV polarization.

As an additional step, the mean ks ($k_{s_{mean}}$) can be estimated from the $k_{s_{HH}}$ and $k_{s_{VV}}$ as follows:

$$k_{s_{mean}} = \frac{k_{s_{HH}} + k_{s_{VV}}}{2}. \quad (25)$$

Fig. 8 shows the GT h_{rms} vs. model-estimated surface roughness plots generated using the $k_{s_{HH}}$ values, $k_{s_{VV}}$ values, and the $k_{s_{mean}}$ values after estimating the model coefficients using the least-square-based curve fitting method. By analyzing Fig. 8, it can be understood that the deviation between the GT h_{rms} and the model-estimated surface roughness are not so high, the root mean square error (RMSE) obtained for the HH polarization is 0.30 mm, for the VV polarization the RMSE is 0.27 mm, and for the HH-VV average the RMSE obtained is also 0.27 mm. This low RMSE indicates that the model coefficients given in Table IV are reliable and can be used in the new model for an accurate estimation of the road surface roughness. From Fig. 8,

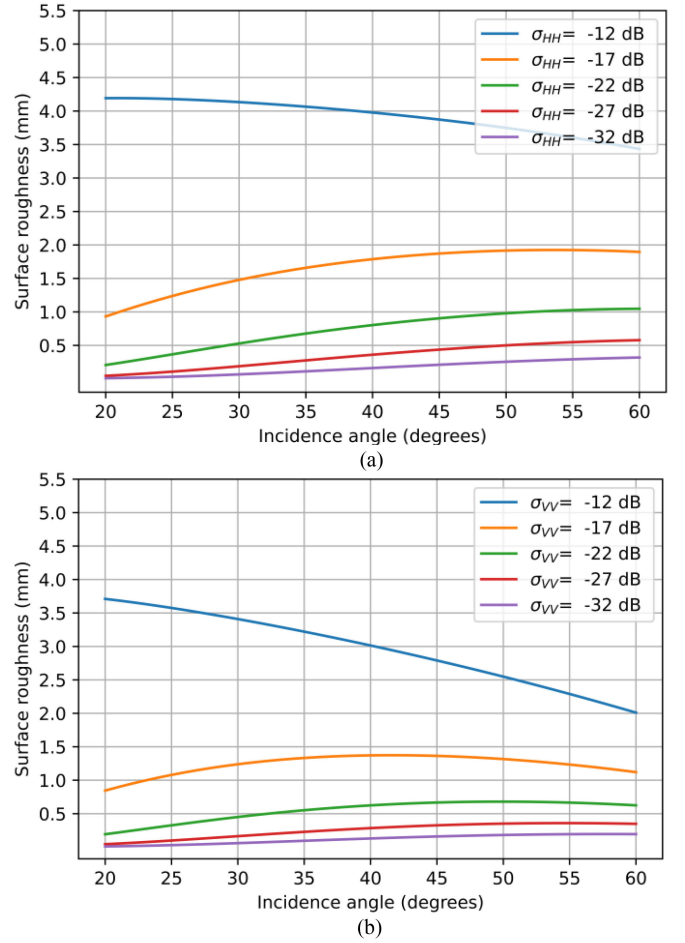


Fig. 9. Model dynamics of the new model. (a) HH polarization. (b) VV polarization.

it can also be observed that the RMSE obtained for the VV polarization is slightly better compared to the RMSE obtained for the HH polarization. Also, the RMSE obtained from the HH–VV average is the same as the RMSE obtained for the VV polarization alone (0.27 mm). So averaging the ks values obtained from the HH and VV polarizations does not provide a better RMSE than using the VV polarization alone. But, the real performance of the new model can only be assessed by estimating the road surface roughness using different datasets acquired from multiple test sites with different acquisition geometries. These results are explained in Section V.

Fig. 9(a) and (b) shows the model dynamics of the new model for HH and VV polarization, respectively. The change in surface roughness values with respect to different incidence angles (θ) and sigma nought (σ°) combinations can be observed in the plots. In Fig. 9(a) and (b), each surface roughness line represents the change in surface roughness with respect to the incidence angle variations when the sigma nought remains constant. From both the plots, it can be observed the changes in surface roughness is small with respect to the incidence angle when the σ° magnitudes are small (e.g., -27 and -32 dB). The change in surface roughness is higher as the incidence angle changes when the σ° magnitude is larger (e.g., -12 dB).

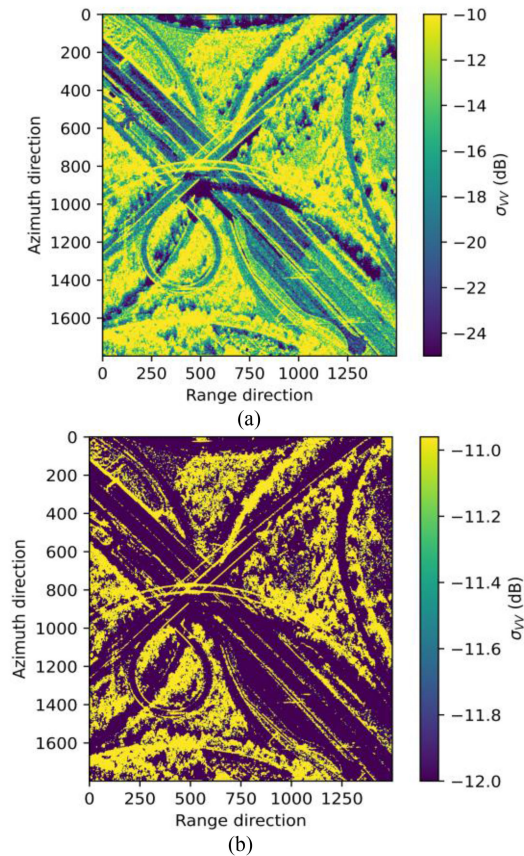


Fig. 10. σ_{VV}^o images. (a) σ_{VV}^o image for Cologne motorway intersection. (b) σ_{VV}^o image showing reflections from lane divider and flyover walls.

E. Sigma Nought and SNR Masking

High sigma nought values not corresponding to the road surface can cause errors in the road surface roughness estimation. Fig. 10(a) shows the σ_{VV}^o image for the Cologne motorway intersection. By analyzing the image, it can be observed that the strong reflection from the lane dividers present in between the roads and also the strong reflection from the flyover walls are visible in yellow color. These strong reflections cause invalid high surface roughness values which need to be eliminated. For this purpose, an upper sigma nought threshold masking technique was implemented. Fig. 10(b) shows the σ_{VV}^o image with sigma nought values higher than -10.96 dB. From Fig. 10(b), it can be understood that all the pixels on the road surface with σ_{VV}^o higher than -10.96 dB corresponds to strong reflections from lane dividers and flyover walls. So all the pixels with σ_{VV}^o greater than -10.96 dB were masked out from the final surface roughness image.

Similar to the high sigma nought values not corresponding to the road surface, the very low SNR pixels can also result in unreliable surface roughness estimation. The sigma nought values obtained from the low SNR pixels are more dominated by the noise than the actual radar signal. The surface roughness values obtained from these pixels are unreliable and do not correspond to the actual GT surface roughness. Therefore, the surface roughness values obtained from the low SNR pixels

should be discarded. The SNR of the dataset can be estimated as follows [42]:

$$\text{SNR}_{pq} = \frac{\sigma_{pq}^o - \lambda_4}{\lambda_4} \quad (26)$$

where SNR_{pq} is the SNR estimated for the pq polarization. σ_{pq}^o is the sigma nought value for the pq polarization and λ_4 is the fourth eigenvalue of the 4×4 coherency matrix which is used for the additive noise removal.

An SNR vs. surface roughness analysis was carried out to estimate the changes in the model-estimated surface roughness as the SNR decreases. For this purpose, a region was identified on the road surface. The actual SNR and the surface roughness for that region were computed using different surface roughness models. After that, simulated complex random Gaussian noise was added to the four polarization channels independently and the SNR was varied from the actual value to lower values and the corresponding changes in the surface roughness were plotted.

The red plot in Fig. 11(a) shows the SNR vs. surface roughness plot for the anisotropy method. By analyzing the plot, it can be observed that the model estimated surface roughness has only small variations for SNR larger than 8.45 dB; and when the SNR falls below 8.45 dB, the surface roughness increases. The green plot in Fig. 11(a) shows the SNR vs. surface roughness plot for the coherency matrix-based method for surface roughness estimation. In this plot also, it can be found that the surface roughness is almost constant (around 2.78 mm) for SNR larger than 9.45 dB. Fig. 11(b) shows the SNR vs. surface roughness plot for the Dubois model. Here, the surface roughness is stable around 0.3 mm for SNR larger than 7.7 dB and then increases as the SNR value drops below 7.7 dB. Fig. 11(c) shows a similar analysis for the new model. From the plot, it can be seen that the surface roughness remains constant at 1.45 mm as long as the SNR is equal to or larger than 8.43 dB. But, only very small deviations are observed for an SNR higher than 5.98 dB. From Fig. 11, it can be generalized that the lowest value of SNR till the surface roughness remains constant indicates the minimum SNR required for each model for a reliable and nonbiased estimation of surface roughness. The surface roughness values of the regions where the SNR is less than these minimum thresholds for each model are invalid and can be neglected to minimize the measurement biases/errors.

F. Geocoding and Google Earth Visualization

The analysis of the road surface condition can be better evaluated by visualizing the surface roughness images in Google Earth. This can help to compare the surface roughness values with the recent high-resolution optical view of the same regions (if available). The block diagram showing the detailed processing scheme for the road surface roughness estimation after performing the preprocessing steps is shown in Fig. 12.

By comparing the overall block diagram for surface roughness estimation shown in Fig. 5 with the detailed block diagram of the processing scheme shown in Fig. 12, it can be seen that the SNR estimation, sigma nought, and SNR masking were performed before generating the surface roughness image as explained in

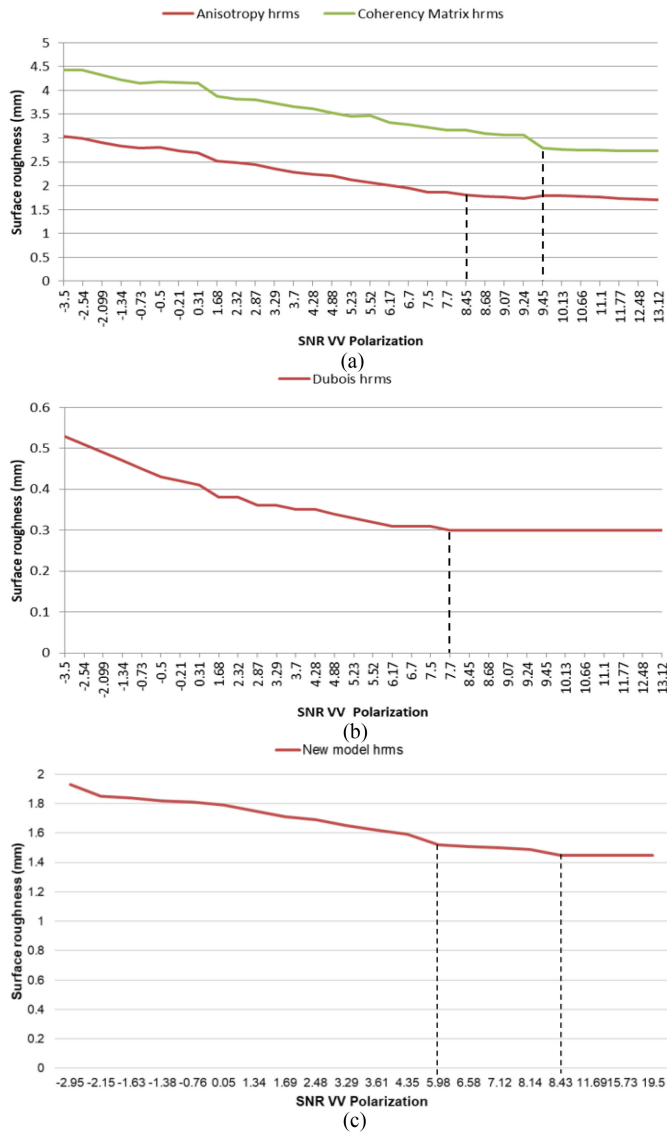


Fig. 11. Surface roughness vs. SNR plots (a) For anisotropy and coherency matrix methods. (b) For Dubois model. (c) For new model.

the previous section. After that, the surface roughness image was further processed to extract the roads and to generate the Google Earth keyhole markup language (KML) files.

To visualize the surface roughness in Google Earth, the surface roughness images generated were geocoded from the slant-range coordinate system to a geographic coordinate system with a grid spacing of 0.25 m. The roads were then extracted from the surface roughness images with the help of the open street map (OSM) road layer [43]. The OSMnx python package was used to download the road layers and all the surface roughness values outside the road layer were masked out from the final surface roughness image [44]. Google Earth KML files were then generated which show the surface roughness results and the road boundaries. In this method, KML files representing surface roughness values of specific roads of interest can be generated by filtering using the type and names of the roads of interest. E.g., the filtering key “Motorway-A4” generates

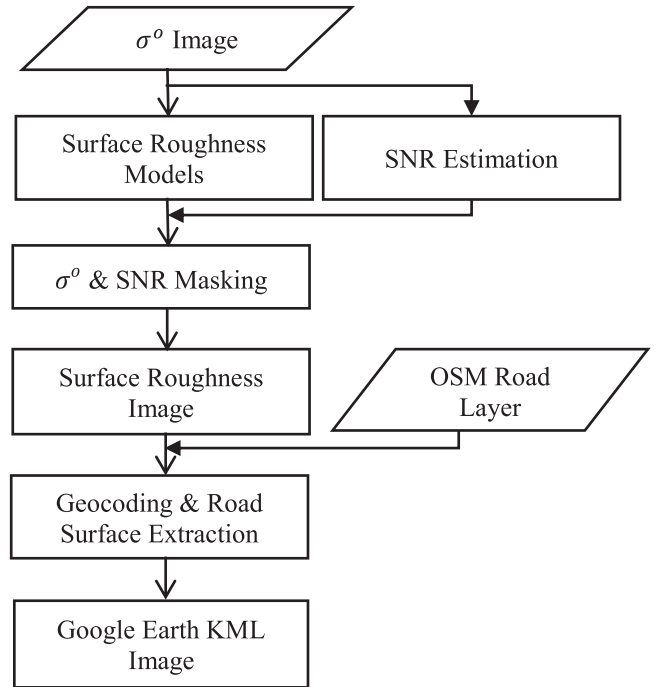


Fig. 12. Block diagram showing the detailed processing scheme.

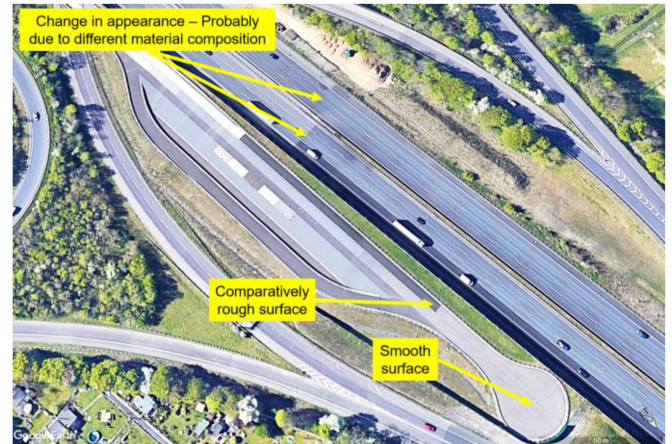


Fig. 13. Google Earth image of duraBAST test site and nearby motorway showing smooth and rough road surfaces.

the surface roughness KML file for the motorway with the name A4.

V. EXPERIMENTAL RESULTS AND DISCUSSION

The surface roughness results obtained using the methods described in the previous section are discussed here.

A. Evaluation of the Surface Roughness Estimation Models

This subsection contains the road surface roughness (h_{rms}) results obtained from the anisotropy method, coherency matrix method, Dubois model, Oh model, and new model.

Fig. 13 shows the Google Earth image of the duraBAST test site near the Cologne motorway intersection. By observing the

image, it can be seen that the duraBAST test site is composed of different road materials having different surface roughness. The smooth and rough regions identified at the duraBAST test site are shown in Fig. 13. Also, a change in road surface color can be observed on the motorway near the duraBAST test site. This can be due to maintenance work done in that region.

Fig. 14(a) shows the surface roughness image generated for the duraBAST test site and the nearby motorway using the anisotropy method without removing the additive noise and Fig. 14(b) shows the surface roughness image generated using the anisotropy method after removing the additive noise. By comparing Fig. 14(a) and (b) with the Google Earth image of the same region shown in Fig. 13, it can be observed that the smooth and rough regions are appearing in the same color. The anisotropy method is unable to differentiate between the smooth and rough road sections even after additive noise removal. Fig. 14(c) and (d) shows the surface roughness images generated using the coherency matrix method before and after removing the additive noise, respectively. From Fig. 14(c), it can be observed that before removing the additive noise, the coherency matrix method is unable to differentiate between the smooth and rough sections of the road. After removing the additive noise, in Fig. 14(d), it can be observed that the result got slightly improved, but, still, the smooth and rough road sections cannot be identified. Even after additive noise removal, the surface roughness image is noisy. Fig. 14(e) and (f) shows the surface roughness results estimated using the Oh 2004 model before and after additive noise removal, respectively. By comparing Fig. 14(e) and (f) with the Google Earth image of the same region shown in Fig. 13, it can be observed that the smooth and rough regions are appearing in the same color. The Oh 2004 method is unable to differentiate between the smooth and rough road sections even after additive noise removal. The surface roughness images generated by the Dubois model before and after additive noise subtraction is shown in Fig. 14(g) and (h), respectively. The effect of additive noise subtraction is not considerably noticeable at this zoom level. In both images, the surface roughness changes shown in Fig. 13 at the duraBAST test site and the motorway can be identified. Fig. 14(i) shows the surface roughness image generated using the new model before additive noise subtraction. By comparing Fig. 14(i) with the Google Earth image shown in Fig. 13 and also with the surface roughness images generated by the Dubois model shown in Fig. 14(g) and (h), it can be found that much smaller changes in the surface roughness variations at the duraBAST test site and also at the motorway are visible in the surface roughness image generated by the new model which are not visible in the surface roughness image generated by the Dubois model. Fig. 14(j) shows the surface roughness image generated by the new model after additive noise subtraction. By comparing Fig. 14(j) with Fig. 14(i), it can be seen that some of the high surface value pixels with yellow color got reduced in Fig. 14(j) after subtracting additive noise. From Fig. 14(a)–(j), it can be found that the Dubois model and the new model produced the best surface roughness results, the surface roughness images generated by the other models were either noisy or were unable to differentiate between smooth and rough road sections.

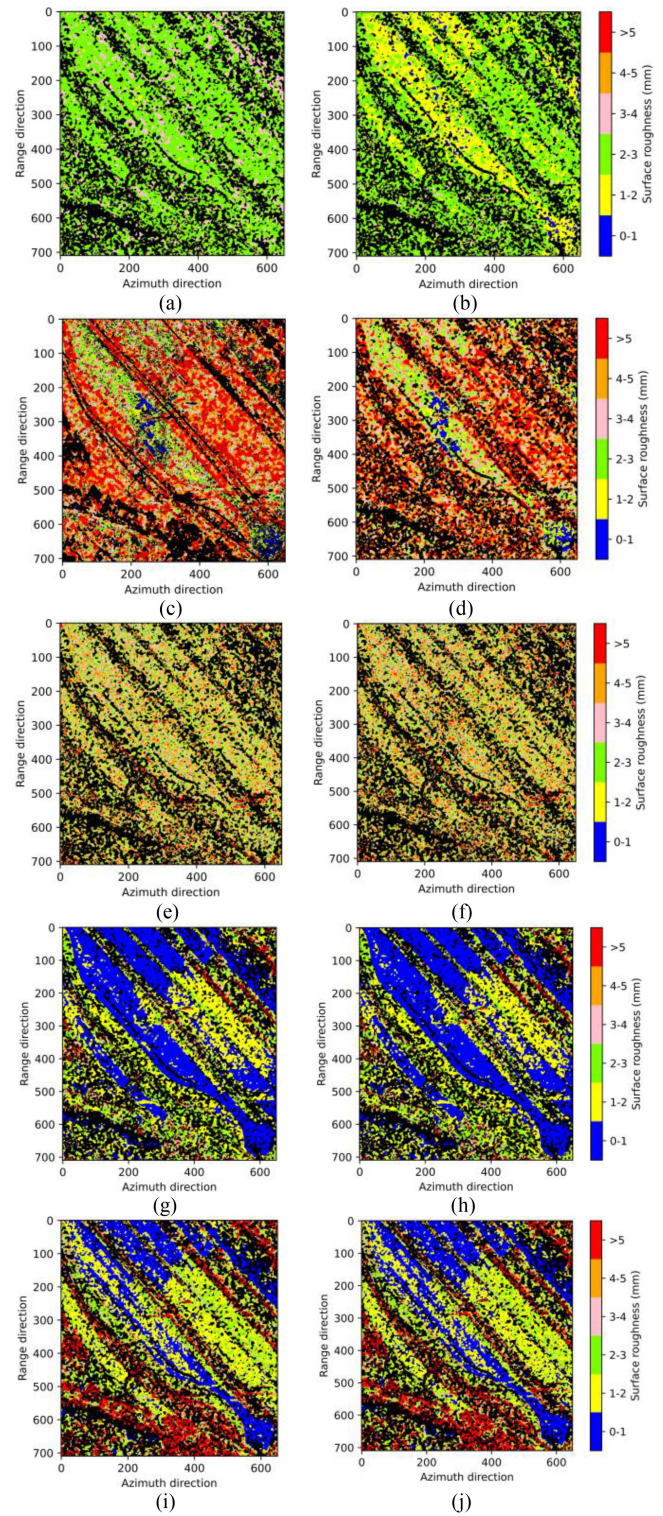


Fig. 14. h_{rms} images. (a) h_{rms} image generated using the anisotropy method before additive noise removal. (b) h_{rms} image generated using the anisotropy method after additive noise removal. (c) h_{rms} image generated using the coherency matrix method before additive noise removal. (d) h_{rms} image generated using the coherency matrix method after additive noise removal. (e) h_{rms} image generated using the Oh 2004 model before additive noise removal. (f) h_{rms} image generated using the Oh 2004 model after additive noise removal. (g) h_{rms} image generated using the Dubois model before additive noise removal. (h) h_{rms} image generated using the Dubois model after additive noise removal. (i) h_{rms} image generated using the new model before additive noise removal. (j) h_{rms} image generated using the new model after additive noise removal.

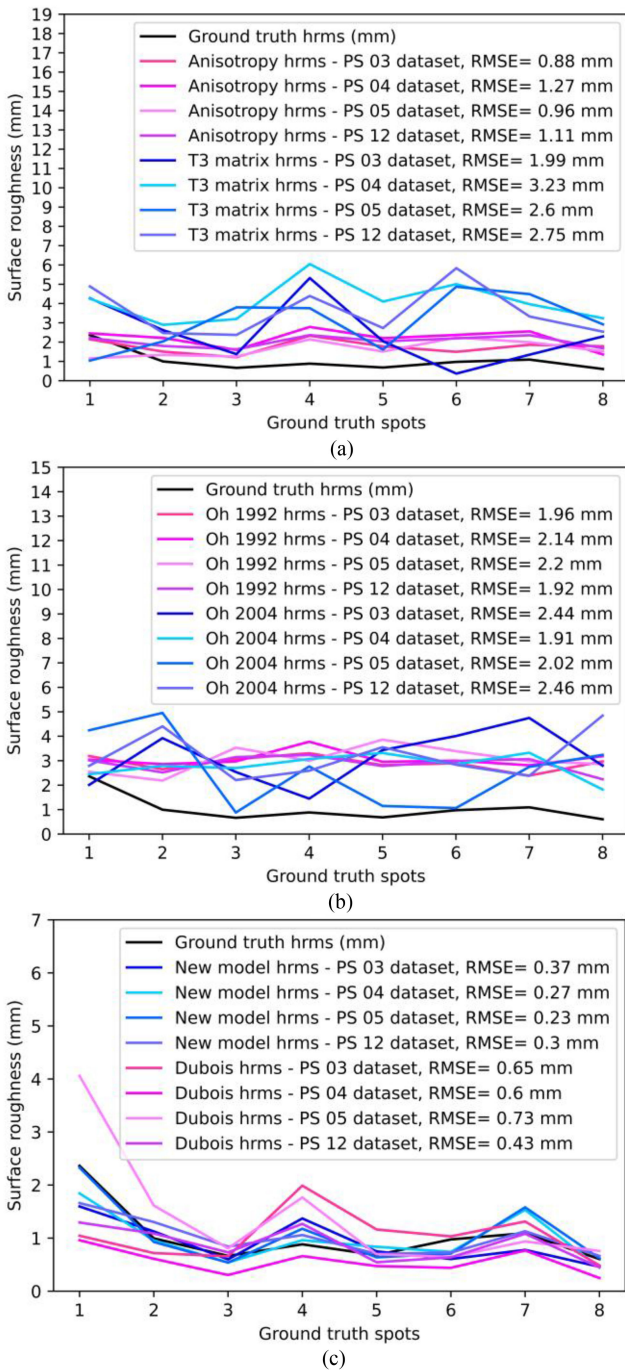


Fig. 15. GT h_{rms} and model estimated surface roughness comparison plots. (a) Anisotropy and coherency matrix method. (b) Oh 1992 and Oh 2004 method. (c) Dubois model and new model.

In Fig. 15, the surface roughness values generated for the GT spots at the Kaufbeuren test site by different models are compared with the GT surface roughness values obtained by laser scanning. The surface roughness plots were generated using the PS 03, PS 04, PS 05, and PS 12 datasets (Fig. 6). Fig. 15(a) shows the surface roughness plots for the GT surface roughness values and the surface roughness values estimated from the anisotropy method and coherency matrix method. By analyzing Fig. 15(a), it can be seen that the surface roughness

TABLE V
COMPARISON OF SURFACE ROUGHNESS RESULTS AT GT SPOTS OBTAINED USING DIFFERENT SURFACE ROUGHNESS ESTIMATION MODELS

GT spot	GT h_{rms} (mm)	Model estimated h_{rms} (PS 03 dataset)					
		Anisotropy	T3 matrix	Oh 1992	Oh 2004	Dubois model	New model
1	2.36	2.14	4.27	3.19	2.01	1.05	1.60
2	0.99	1.50	2.61	2.65	3.92	0.72	1.12
3	0.66	1.22	1.38	3.06	2.54	0.66	0.60
4	0.88	2.33	5.32	3.31	1.45	1.99	1.37
5	0.68	1.78	2.04	2.82	3.43	1.16	0.74
6	0.98	1.50	0.37	2.90	4.01	1.03	0.61
7	1.09	1.86	1.35	2.39	4.75	1.31	0.78
8	0.61	1.79	2.29	2.97	2.80	0.49	0.46
RMSE (mm)		0.88	1.99	1.96	2.44	0.65	0.37

values estimated by the anisotropy model at the smooth GT spots (low surface roughness spots) were highly overestimated and the model estimated surface roughness values at the rough GT spots (high surface roughness spots) were underestimated. For the coherency matrix method, the surface roughness values obtained at both the rough and smooth spots were highly overestimated. Table V shows the comparison between the GT surface roughness values and the model estimated surface roughness values for the PS 03 dataset. From Table V, it can be found that the RMSE obtained for the anisotropy method is 0.88 and 1.99 mm for the coherency matrix method. Fig. 15(b) shows the surface roughness plots generated using Oh 1992 model and Oh 2004 model. By observing the plots, it can be understood that the surface roughness values estimated by both the Oh 1992 model and Oh 2004 model were overestimated at both the smooth and rough GT spots. From Table V, it can also be seen that the RMSE obtained for the Oh 1992 model is 1.96 and 2.44 mm for the Oh 2004 model. From Fig. 15(a) and (b), it can be understood that the model estimated surface roughness plots are not correlated with the GT surface roughness plots.

By comparing the Dubois model estimated surface roughness plots with the GT plot, it can be seen that some of the datasets show an underestimation at the GT spots and some other datasets show an overestimation. But, it can be seen that the plots are correlated and follow the same trend of the GT surface roughness plot. From Table V, it can be seen that the RMSE obtained for the Dubois model using the PS 03 dataset is 0.65 mm which is lower compared to the abovementioned models. By comparing the surface roughness plots estimated using the new model with the GT surface roughness plot, it can be seen that the deviations are the lowest between the plots. From Table V also, it can be seen that the RMSE obtained for the new model using the PS 03 dataset is 0.37 mm, which is the lowest RMSE obtained from all the models. The PS 03 is used for Table V

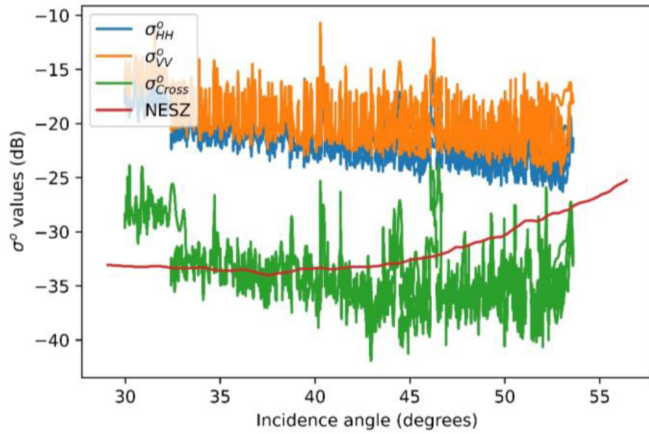


Fig. 16. Sigma nought vs. incidence angle plot.

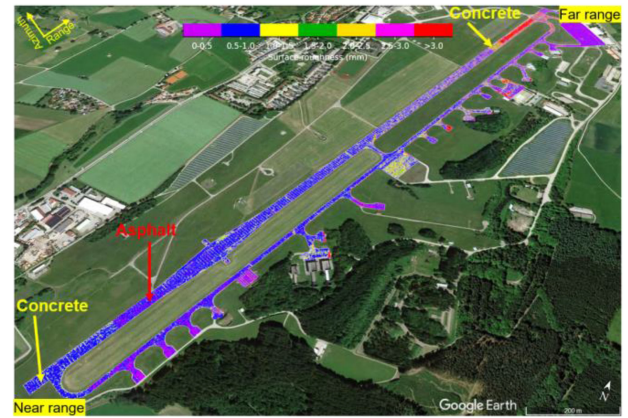
because this dataset was not used for estimating the new model coefficients.

Sigma nought values of the road surface for different polarizations were compared with the noise equivalent sigma zero (NESZ) of the SAR system to understand the performance differences of different surface roughness estimation models.

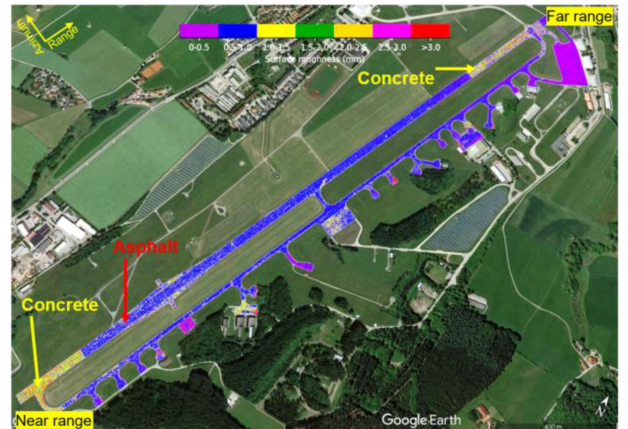
Fig. 16 shows the sigma nought vs. incidence angle plot along the range direction. The sigma nought values were extracted from the linear Kaufbeuren runway. In Fig. 16, the blue line represents the sigma nought magnitude plot for the HH polarization, the orange line represents the sigma nought magnitude plot for the VV polarization, the green line represents the sigma nought magnitude plot for the cross-polarization, and the red line shows the NESZ threshold plot along the range direction. From Fig. 16, it can be observed that the sigma nought magnitude plots for the HH and VV polarization stay above the NESZ threshold from near range to far range. But, the sigma nought magnitude for the cross-polarization falls below the NESZ as the incidence angle increases. Since the sigma nought magnitude for the cross-polarization falls below the NESZ threshold for the road surface, the cross-polarization channels are not reliable for the road surface roughness estimation. The anisotropy method, coherency matrix method, Oh 1992 model, and the Oh 2004 models require the cross-polarization channels for the surface roughness estimation. This is the reason for the unreliable surface roughness estimation from these models. On the other hand, the Dubois model and the new model require only the copolarization channels for the surface roughness estimation. This is the reason for the better performance of the Dubois model and the new model for surface roughness estimation.

B. Performance of the New Model

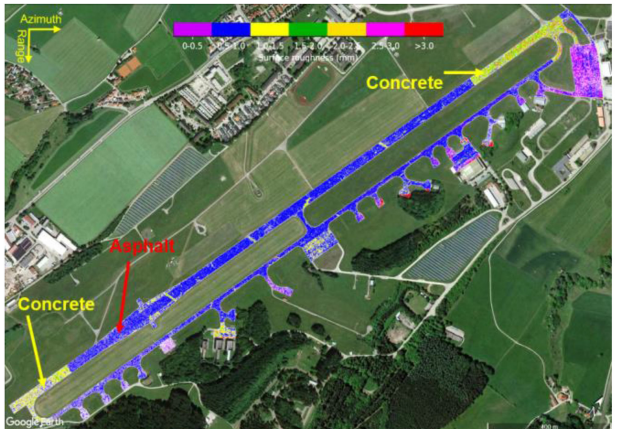
From the results discussed in the previous section, it can be understood that the Dubois model and the new model performed better compared to the other models. But, the surface roughness values estimated by the Dubois model have an incidence angle



(a)



(b)



(c)

Fig. 17. Surface roughness images of the Kaufbeuren test site. (a) Dubois model. (b) New model using training data. (c) New model using testing data.

dependency which led to the development of a new semi-empirical model based on the assumptions from the Dubois model.

Fig. 17(a) shows the surface roughness image of the Kaufbeuren test site estimated using the Dubois model. The surface roughness image is visualized in Google Earth after geocoding and masking out the regions outside the runway, taxiway, and parking areas. The near range and far range are marked in the image. As discussed in the study area section, both ends of the runway are made of concrete and the middle region is made of

asphalt. But in Fig. 17(a), it can be observed that at the near range the Dubois model is unable to differentiate between concrete and asphalt. Both concrete and asphalt appear in blue indicating similar surface roughness. But, at the far range, the Dubois model can clearly distinguish between asphalt and concrete. The asphalt regions are appearing mainly in blue color and the concrete regions are appearing in yellow and red color. The red color is due to the rugged surface present at the end of the runway to provide better braking for the aircraft. Also, a gradient increase in the surface roughness can be observed from near range to far range at the asphalt regions. All these observations point out that the surface roughness values estimated by the Dubois model are influenced by the incidence angle and the model sensitivity to surface roughness is less at the near range.

The new model is developed based on the Dubois model assumptions to minimize this incidence angle dependency problem and also to improve the overall accuracy of the road surface roughness estimation. Since the new model coefficients are estimated using the GT data obtained from the road surface itself, it is expected to perform better compared to the other models which are originally trained for the soil roughness estimation. Fig. 17(b) shows the surface roughness image generated for the Kaufbeuren test site using the new model. Fig. 17(a) and (b) was generated using the PS 05 dataset. The acquisition geometry of the PS 05 dataset is shown in Fig. 6. This dataset was one of the three datasets used for estimating the new model coefficients. So for the new model, the PS 05 dataset can be considered as a training dataset. By comparing Fig. 17(b) with the surface roughness image generated using the Dubois model shown in Fig. 17(a), it can be seen that in the surface roughness image generated using the new model, the concrete regions at both ends of the runway are showing a high value of surface roughness indicated by the yellow color and the asphalt regions are showing a low value of surface roughness indicated by the blue color. From this result, it can be clearly understood that the new model can distinguish between concrete and asphalt at both near range and far range which may also have different surface roughness. Also, if we look at the asphalt regions from near range to far range, it can be observed that the influence of incidence angle on surface roughness variations has reduced considerably. Fig. 17(c) shows the surface roughness image generated using the new model using the PS 03 dataset which was not part of the model coefficients estimation and has a different acquisition geometry (Fig. 6). So this dataset can be considered as a testing dataset. By comparing Fig. 17(c) with Fig. 17(b), it can be found that both the images look very similar with asphalt appearing in blue color and concrete appearing in yellow color. So the new model performs satisfactorily with both the training and testing data.

Table VI shows the comparison between the GT surface roughness values and the surface roughness values obtained using the Dubois model and the new model. By analyzing the table, it can be understood that the Dubois model has an RMSE of 0.73 mm. The new model has an RMSE of 0.23 mm for the training data and the testing data, the RMSE is 0.37 mm. So in

TABLE VI
COMPARISON OF SURFACE ROUGHNESS RESULTS AT GT SPOTS OBTAINED USING DUBOIS MODEL AND NEW MODEL

GT spot	GT h_{rms} (mm)	Dubois model	New model (training data)	New model (testing data)
1	2.36	4.06	2.33	1.60
2	0.99	1.61	0.93	1.13
3	0.66	0.81	0.54	0.60
4	0.88	1.77	1.17	1.37
5	0.68	0.69	0.64	0.75
6	0.98	0.64	0.71	0.61
7	1.09	0.94	1.58	0.78
8	0.61	0.75	0.62	0.46
RMSE (mm)		0.73	0.23	0.37

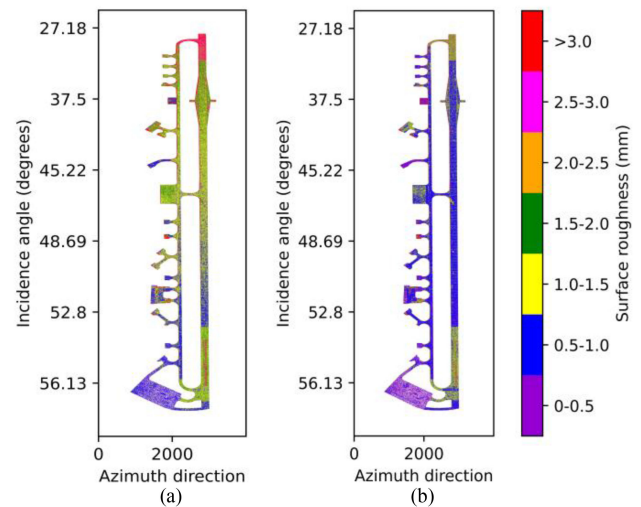


Fig. 18. Surface roughness images of the Kaufbeuren test site (PS 05 dataset). (a) New model without $\sin(\theta)$ term. (b) New model with $\sin(\theta)$ term.

both cases, the new model can provide a better surface roughness estimate compared to the Dubois model.

The $\sin(\theta)$ term is added in the new model (22) to counter its sensitivity to the incidence angle. Fig. 18(a) shows the surface roughness image generated using the new model without considering the $\sin(\theta)$ term. The incidence angle sensitivity on the surface roughness can be clearly seen in Fig. 18(a). The concrete regions of the runway at the near range are appearing in red and magenta color indicating higher values of surface roughness and the concrete regions of the runway at the far range are appearing in green color indicating comparatively lower values of surface roughness. The smooth asphalt regions of the runway are also showing higher values of surface roughness at the near range that gradually decrease toward far range. Fig. 18(b) shows the surface roughness image generated using the new model after including the $\sin(\theta)$ term. By comparing Fig. 18(b) with Fig. 18(a), it can be seen that the sensitivity of surface roughness to the incidence angle is considerably reduced in Fig. 18(b). The concrete regions of the runway at both near and far range are appearing in yellow

color indicating a similar range of surface roughness values. The smooth asphalt regions of the runway are also appearing in blue color and the gradient change in surface roughness from near to far range is considerably reduced. The addition of the $\sin(\theta)$ term has a crucial role in the superior performance of the new model and it can be verified by comparing the results shown in Figs. 17 and 18.

C. Influence of SNR and Sigma Nought

As discussed in the methodology section, an upper sigma nought threshold masking and a lower SNR threshold masking are required to remove the unreliable surface roughness values from the surface roughness images.

Fig. 19(a) shows the surface roughness image generated using the new model for the Wolfsburg motorway intersection at

Braunschweig, Germany, without performing sigma nought and SNR masking. The zoomed view in the figure shows a portion of the motorway where a change in surface roughness can be observed. This sudden change in surface roughness at the motorway may be due to a maintenance work done in that region. In the zoomed view, it can be seen that two red stripes are present across the road indicating high surface roughness values. These red stripes are caused due to the strong backscatter signal from the overhead signboard present there and do not correspond to the actual surface roughness of that location. Also, the green color present in between the two lanes of the motorway is caused due to the strong reflection from the lane dividers separating the two roads. An upper sigma nought threshold masking can be done to remove this kind of anomalies from the surface roughness image. Fig. 19(b) shows the surface roughness image generated after performing the upper sigma nought threshold masking. In Fig. 19(b), all the pixels with sigma nought values higher than -10.96 dB were masked out to remove strong reflections from signboards, lane dividers, etc. If we compare the zoomed view shown in Fig. 19(b) with the zoomed view shown in Fig. 19(a), it can be observed that the two red stripes present in Fig. 19(a) due to the strong reflection from the signboards are not visible in Fig. 19(b) after upper sigma nought threshold masking. Also, it can be seen that the green color present in between the lanes due to the reflection from the lane dividers is also removed in Fig. 19(b). So the upper sigma nought masking technique is an effective way to mask out unreliable pixels from the surface roughness image caused due to strong reflecting targets. Even after upper sigma nought threshold masking, the low SNR pixels can still lead to unreliable surface roughness values. So all the pixels with SNR less than 5.98 dB were masked out from the surface roughness image. Fig. 19(c) shows the surface roughness image after performing both upper sigma nought threshold masking and lower SNR threshold masking. By comparing Fig. 19(b) with Fig. 19(c), it can be seen that some of the pixels corresponding to the blue color got removed in Fig. 19(c). These pixels were having an SNR of less than 5.98 dB. Both upper sigma nought threshold masking and low SNR threshold masking can be applied together to minimize the unreliable values from the surface roughness images.

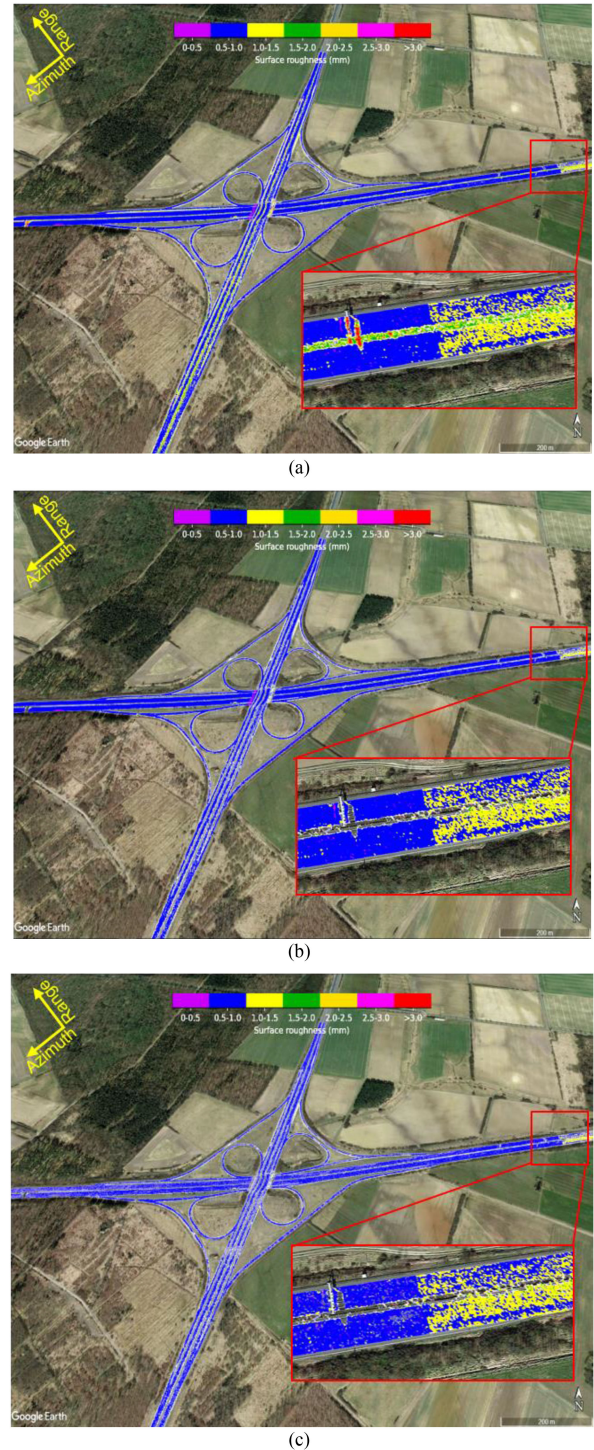


Fig. 19. Surface roughness images of the Wolfsburg motorway intersection at Braunschweig (a) Without sigma nought and SNR masking. (b) With sigma nought masking. (c) With both sigma nought and SNR masking.

D. Single Surface Roughness Image From Multiple Datasets

The surface roughness images generated from a single dataset can contain unreliable surface roughness values caused due to shadow areas, speckle, low SNR regions, and incidence angle. To minimize these errors, the surface roughness images generated from multiple datasets having different acquisition geometries

can be combined to generate a single surface roughness image. The highest SNR method or multidataset averaging method can be used to generate a single surface roughness image from multiple datasets.

In the highest SNR method, the geocoded surface roughness matrices and SNR matrices were generated for all the available datasets. A pixelwise SNR search is then done through all the available SNR matrices to identify the highest SNR dataset for that particular pixel in the matrix. The surface roughness value estimated from this highest SNR dataset is then used for that particular pixel. This process is then repeated for all the pixels in the geocoded grid. In this method, each pixel of the final surface roughness matrix will be filled with the value from the highest SNR dataset. In the multidataset averaging method, the single surface roughness image is generated by performing pixelwise averaging of the surface roughness results generated from multiaspect angle datasets. The multidataset averaging is performed after upper threshold sigma nought masking and lower SNR threshold masking.

Fig. 20(a) shows the surface roughness image generated using the new model from a single dataset which was not used for training the new model (PS 03 dataset). The concrete regions present at both ends of the runway can be clearly distinguished from the asphalt regions. The concrete regions at the ends of the runway can be seen in yellow color, while the asphalt regions mainly appear in blue. The two zoomed views in the image show the portions of the runway where some repair works were carried out. The regions where the repairs were done are appearing in yellow color indicating higher surface roughness.

Fig. 20(b) shows the single surface image generated from multiple datasets using the highest SNR method. By comparing Fig. 20(b) with Fig. 20(a), it can be observed that much finer details are visible in Fig. 20(b) than in Fig. 20(a). More details of the runway can be seen in the zoomed view shown in Fig. 20(b) than in the zoomed view shown in Fig. 20(a). But, the effect of local backscatter variations seems to be more dominant in the single surface image generated using the highest SNR method. These local backscatter variations are caused due to the oriented features on the road surface which can lead to high backscattering only from certain aspect angles.

Fig. 20(c) shows the single surface roughness image generated from multiple datasets using the multidataset averaging method. By comparing Fig. 20(c) with Fig. 20(b) and Fig. 20(a), it can be seen that the multidataset averaging image looks much smoother compared to the other two images. All the local variabilities present in the first two images were smoothed out due to this multidataset averaging. From the zoomed view shown in Fig. 20(c), it can be found that the result looks much better than the results shown in Fig. 20(a) and (b). The repair works done on the runway can be seen in yellow color and the surrounding regions are appearing in blue color without many variations. The multidataset averaging procedure has reduced the effect of speckle in the surface roughness image.

Table VII shows the comparison between the GT surface roughness, surface roughness estimated from a single dataset using the new model, single surface roughness image generated

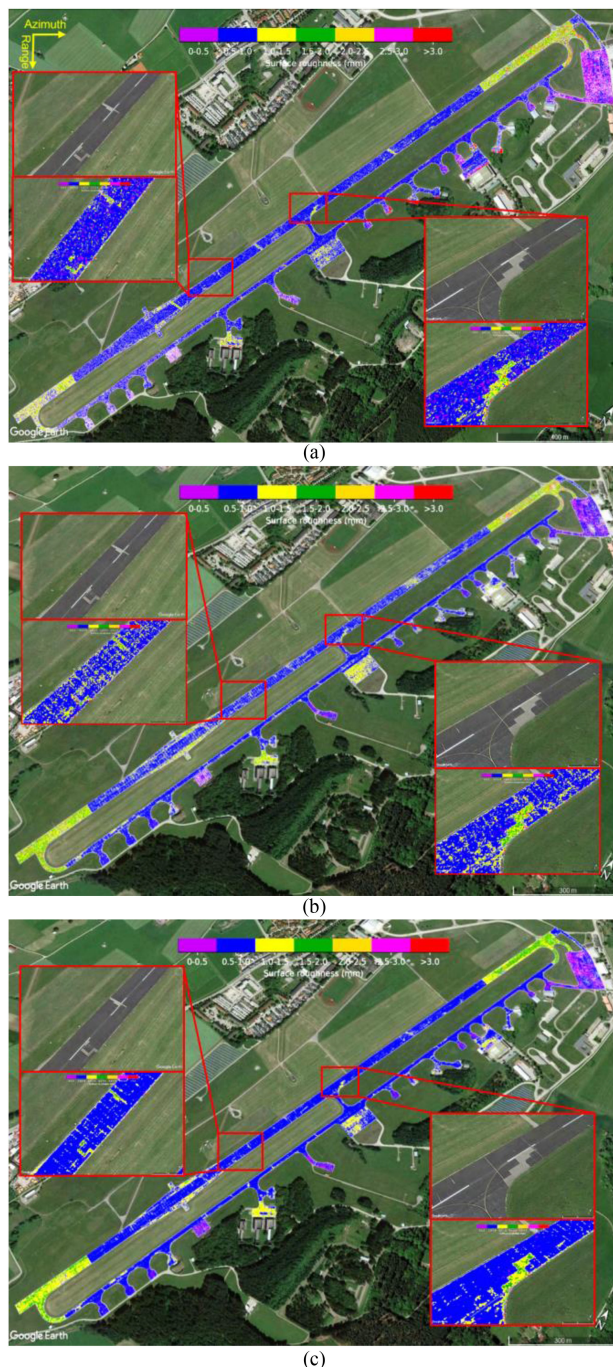


Fig. 20. Surface roughness images of the Kaufbeuren test site. (a) Surface roughness image generated using the new model. (b) Single surface image generated from multiple datasets using the highest SNR method. (c) Single surface roughness image generated from multiple datasets using the multidataset averaging method.

using the highest SNR method, and the single surface roughness image generated using the multidataset averaging method. The RMSE obtained from the new model for the GT spots is 0.37 mm. For the highest SNR method, the RMSE obtained is 0.43 mm. So the single surface image generated from multiple datasets using the highest SNR method has a higher RMSE than the surface roughness image generated from a single dataset. This is because

TABLE VII
COMPARISON OF SURFACE ROUGHNESS RESULTS AT GT SPOTS OBTAINED USING NEW MODEL AND MULTI DATASET METHODS

GT spot	GT h_{rms} (mm)	Surface roughness from a single dataset	Highest SNR method	Multi dataset averaging method
1	2.36	1.60	1.76	1.78
2	0.99	1.13	1.60	1.14
3	0.66	0.60	0.75	0.60
4	0.88	1.37	1.73	1.40
5	0.68	0.75	1.02	0.80
6	0.98	0.61	0.79	0.79
7	1.09	0.78	1.74	1.28
8	0.61	0.46	0.58	0.59
RMSE (mm)		0.37	0.43	0.29

the highest SNR method is very sensitive to the speckle and local variations in the datasets. For the multidataset averaging method, the RMSE obtained is 0.29 mm. In this case, RMSE is much lower compared to the highest SNR method and single dataset method. From Fig. 20 and Table VII, it can be clearly understood that generating a single surface roughness image from multiple datasets using the multidataset averaging technique can generate surface roughness images with fewer local variations and low RMSE.

VI. CONCLUSION

This article proposes a novel approach for the periodic monitoring of road surface roughness using high-resolution airborne PolSAR datasets. Compared to the conventional methods, the road surface roughness estimation using airborne PolSAR datasets is efficient, less time consuming, and cost-effective for a country-wide scale application. The X-band airborne PolSAR datasets used in this article show very good sensitivity to the road surface roughness and thus show great potential for wide-area road surface roughness estimation. But, the estimation of road surface roughness from the SAR datasets is challenging due to the low radar backscatter obtained from the smooth road surface. Because of this reason, the additive noise present in the datasets should be minimized before estimating the road surface roughness. In this article, the additive noise is minimized using the eigenvalue-based coherency matrix method. The existing polarimetric anisotropy-based model, coherency matrix-based model, and the semi-empirical Oh models were found to be not reliable for road surface roughness estimation because of their dependency on noise dominant cross-polarization channels. The Dubois model is found to provide a better estimate of the road surface roughness because of its dependency only on copolarization channels. But, the Dubois model is biased due to its sensitivity to incidence angle variations. A new semi-empirical model is proposed in this article for the HH and VV polarizations based on the assumptions from the Dubois

model. The road surface roughness results obtained from the new model show a very good correlation with GT surface roughness data. Upper sigma nought threshold masking and lower SNR threshold masking were implemented to eliminate unreliable surface roughness values. Finally, the surface roughness images were generated only for the road surfaces and visualized in Google Earth with the help of the road layers from the OSM. Also, it is interesting to note that the new model requires only HH or VV polarization for the road surface roughness estimation. The principle of PolSAR was required only for additive noise attenuation. So it is possible to estimate the road surface roughness using a cheaper and less complex single-pol SAR system. In this case, a different noise attenuation method that requires only single-pol data needs to be used. In the next phase of this article, further experiments are planned using an airborne polarimetric Ka-band SAR which, due to the smaller wavelength, will be more sensitive to the surface roughness differences. The upcoming Ka-band datasets can potentially also be used to monitor the unevenness of the road surfaces and possibly estimate the International Roughness Index parameter. It is also planned to test the applicability of the new model on spaceborne SAR data, especially on high-resolution staring spotlight data acquired with TerraSAR-X and/or TanDEM-X. But, in the case of spaceborne SAR datasets, there can occur additional difficulties in the road surface roughness estimation due to the possibility of large radar shadow regions at certain locations and the opportunities to acquire datasets from multiple aspect angles are typically also limited. Therefore, the study area should be limited to regions where radar shadowing is minimal. Also, the lower SNR threshold masking technique discussed in this article can still be applied on the spaceborne SAR datasets to filter out the unreliable surface roughness estimates from the shadow regions. Even though there are some additional challenges, the use of the spaceborne SAR datasets can help in wide-area road surface roughness estimation in the future.

ACKNOWLEDGMENT

The authors would like to thank Martin Keller, Microwaves and Radar Institute, German Aerospace Center for performing the ground truth data collection campaign at the Kaufbeuren test site.

REFERENCES

- [1] J. Hofmöckel, J. Masino, J. Thumm, E. Sax, and F. Gauterin, "Multiple vehicle fusion for a robust road condition estimation based on vehicle sensors and data mining," *Cogent Eng.*, vol. 5, no. 1, pp. 1–15, 2018.
- [2] J. Matijošius, A. V. Vasiliauskas, V. Vasilienė-Vasiliauskienė, and Ž. Krašodomskis, "The assessment of importance of the factors that predetermine the quality of a service of transportation by road vehicles," *Procedia Eng.*, vol. 134, pp. 422–429, 2016.
- [3] A. Babu and S. V. Baumgartner, "Road surface roughness estimation using polarimetric SAR data," in *Proc. 21st Int. Radar Symp.*, 2020, pp. 281–285.
- [4] A. Babu and S. V. Baumgartner, "Road surface quality assessment using polarimetric airborne SAR," in *Proc. IEEE Radar Conf.*, 2020, pp. 1–5.
- [5] A. Babu, S. V. Baumgartner, and G. Krieger, "Road surface condition monitoring using fully polarimetric airborne SAR data," in *Proc. 13th Eur. Conf. Synthetic Aperture Radar*, 2021, pp. 1–6.

- [6] C. Y. Chan, B. Huang, X. Yan, and S. Richards, "Investigating effects of asphalt pavement conditions on traffic accidents in Tennessee based on the pavement management system (PMS)," *J. Adv. Transp.*, vol. 44, no. 3, pp. 150–161, 2010.
- [7] R. Ghandour, A. Victorino, M. Doumiati, and A. Charara, "Tire/road friction coefficient estimation applied to road safety," in *Proc. 18th Mediterranean Conf. Control Automat.*, 2010, pp. 1485–1490.
- [8] P. Wriggers and J. Reinelt, "Multi-scale approach for frictional contact of elastomers on rough rigid surfaces," *Comput. Methods Appl. Mech. Eng.*, vol. 198, pp. 1996–2008, 2009.
- [9] H. Liu, Z. Zhang, D. Guo, L. Peng, Z. Bao, and W. Han, "Research progress on characteristic technique of pavement micro-texture and testing technology of pavement skid resistance at home and abroad," in *Proc. Int. Conf. Remote Sens., Environ. Transp. Eng.*, 2011, pp. 4368–4372.
- [10] O. Frolova and B. Salaiová, "Analysis of road cover roughness on 'control' road section with crumb tire rubber," *Procedia Eng.*, vol. 190, pp. 589–596, 2017.
- [11] M.-T. Do and V. Cerezo, "Road surface texture and skid resistance," *Surf. Topogr. Metrol. Properties*, vol. 3, no. 4, Oct. 2015, Art. no. 43001.
- [12] I. Hajnsek, "Inversion of surface parameters using polarimetric SAR," Ph.D. dissertation, Fac. Chemistry Geosci., Friedrich Schiller Univ., Jena, Germany, 2001.
- [13] T. Jagdhuber, "Soil parameter retrieval under vegetation cover using SAR polarimetry," Ph.D. dissertation, Fac. Math. Natural Sci., Univ. Potsdam, Potsdam, Germany, 2012.
- [14] M. Acosta, S. Kanarachos, and M. Blundell, "Road friction virtual sensing: A review of estimation techniques with emphasis on low excitation approaches," *Appl. Sci.*, vol. 7, no. 12, 2017, Art. no. 1230.
- [15] *Michelin: The Tyre Grip*. Clermont-Ferrand, France: Société de Technologie Michelin, 2004.
- [16] Q. Li, F. Qiao, and L. Yu, "Impacts of pavement types on in-vehicle noise and human health," *J. Air Waste Manage. Assoc.*, vol. 66, no. 1, pp. 87–96, 2016.
- [17] K. Laubis, "Crowd-based road surface monitoring and its implications on road users and road authorities," Ph.D. dissertation, Fac. Econ., Karlsruhe Inst. Technol., Karlsruhe, Germany, 2017.
- [18] F. J. Meyer, O. A. Ajadi, and E. J. Hoppe, "Studying the applicability of X-band SAR data to the network-scale mapping of pavement roughness on US roads," *Remote Sens.*, vol. 12, no. 9, 2020, Art. no. 1207.
- [19] F. J. Meyer, O. A. Ajadi, and E. Hoppe, "Network-scale pavement roughness mapping using spaceborne high-resolution X-band SAR data," in *Proc. IEEE Int. Geosci. Remote Sens. Symp.*, 2017, pp. 1558–1561.
- [20] *Federal Highway Research Institute*, "BASt special," Bergisch Gladbach, Germany: Bundesanstalt für Straßenwesen (BASt), Research Controlling and Press and Public Relations, 2017.
- [21] R. Horn, A. Nottensteiner, A. Reigber, J. Fischer, and R. Scheiber, "F-SAR — DLR's new multifrequency polarimetric airborne SAR," in *Proc. IEEE Int. Geosci. Remote Sens. Symp.*, 2009, pp. II-902–II-905.
- [22] M. Keller, J. Fischer, and M. Jäger, *DLR's Airborne SAR F-SAR Product Description*. Oberpfaffenhofen, Germany: Microw. Radar Inst., German Aerosp. Center, 2019.
- [23] F. Mattia *et al.*, "The effect of surface roughness on multifrequency polarimetric SAR data," *IEEE Trans. Geosci. Remote Sens.*, vol. 35, no. 4, pp. 954–966, Jul. 1997.
- [24] N. Baghdadi and M. Zribi, "Evaluation of radar backscatter models IEM, OH and Dubois using experimental observations," *Int. J. Remote Sens.*, vol. 27, no. 18, pp. 3831–3852, 2006.
- [25] J. Shi, J. Wang, A. Y. Hsu, P. E. O'Neill, and E. T. Engman, "Estimation of bare surface soil moisture and surface roughness parameter using L-band SAR image data," *IEEE Trans. Geosci. Remote Sens.*, vol. 35, no. 5, pp. 1254–1266, Sep. 1997.
- [26] F. Argenti, A. Lapini, L. Alparone, and T. Bianchi, "A tutorial on speckle reduction in synthetic aperture radar images," *IEEE Geosci. Remote Sens. Mag.*, vol. 1, no. 3, pp. 6–35, Sep. 2013.
- [27] A. S. Yommy, R. Liu, and S. Wu, "SAR image despeckling using refined lee filter," in *Proc. 7th Int. Conf. Intell. Human-Mach. Syst. Cybern.*, 2015, pp. 260–265.
- [28] I. Hajnsek, K. P. Papathanassiou, and S. R. Cloude, "Removal of additive noise in polarimetric eigenvalue processing," in *Proc. IEEE Scanning Present Resolving Future. Int. Geosci. Remote Sens. Symp.*, 2001, pp. 2778–2780.
- [29] M. M. Espeseth, S. Skrunes, C. Brekke, and M. Johansson, "The impact of additive noise on polarimetric radarsat-2 data covering oil slicks," in *Proc. IEEE Int. Geosci. Remote Sens. Symp.*, 2019, pp. 5756–5759.
- [30] A. Freeman, "The effects of noise on polarimetric SAR data," in *Proc. IEEE Int. Geosci. Remote Sens. Symp.*, 1993, pp. 799–802.
- [31] E. Pottier, J.-S. Lee, and L. Ferro-Famil, *Advanced Concepts in Polarimetry — Part I*. Washington, DC, USA: NAVAL Research Lab., 2004, pp. 21–22.
- [32] J. A. Richards, *Remote Sensing With Imaging Radar*. Berlin, Germany: Springer, 2009.
- [33] Y. Oh, K. Sarabandi, and F. T. Ulaby, "An empirical model and an inversion technique for radar scattering from bare soil surfaces," *IEEE Trans. Geosci. Remote Sens.*, vol. 30, no. 2, pp. 370–381, Mar. 1992.
- [34] Y. Oh, "Quantitative retrieval of soil moisture content and surface roughness from multipolarized radar observations of bare soil surfaces," *IEEE Trans. Geosci. Remote Sens.*, vol. 42, no. 3, pp. 596–601, Mar. 2004.
- [35] P. C. Dubois, J. van Zyl, and T. Engman, "Measuring soil moisture with imaging radars," *IEEE Trans. Geosci. Remote Sens.*, vol. 33, no. 4, pp. 915–926, Jul. 1995.
- [36] D. G. Long and F. Ulaby, *Microwave Radar and Radiometric Remote Sensing*. Ann Arbor, MI, USA: Univ. Michigan Press, 2014.
- [37] N. Baghdadi *et al.*, "A new empirical model for radar scattering from bare soil surfaces," *Remote Sens.*, vol. 8, no. 11, pp. 1–14, 2016.
- [38] M. Beauchemin, K. P. B. Thomson, and G. Edwards, "Modelling forest stands with MIMICS: Implications for calibration," *Can. J. Remote Sens.*, vol. 21, no. 4, pp. 518–526, 1995.
- [39] N. Baghdadi, M. Bernier, R. Gauthier, and I. Neeson, "Evaluation of C-band SAR data for wetlands mapping," *Int. J. Remote Sens.*, vol. 22, no. 1, pp. 71–88, 2001.
- [40] M. R. Sahebi, J. Angles, and F. Bonn, "A comparison of multi-polarization and multi-angular approaches for estimating bare soil surface roughness from spaceborne radar data," *Can. J. Remote Sens.*, vol. 28, no. 5, pp. 641–652, 2002.
- [41] N. Baghdadi, N. Holah, and M. Zribi, "Soil moisture estimation using multi-incidence and multi-polarization ASAR data," *Int. J. Remote Sens.*, vol. 27, no. 10, pp. 1907–1920, 2006.
- [42] M. M. Espeseth, C. Brekke, C. E. Jones, B. Holt, and A. Freeman, "The impact of system noise in polarimetric SAR imagery on oil spill observations," *IEEE Trans. Geosci. Remote Sens.*, vol. 58, no. 6, pp. 4194–4214, Jun. 2020.
- [43] P. Mooney and M. Minghini, "A review of openstreetmap data," in *Mapping and the Citizen Sensor*. G. M. Foody, L. See, and P. Mooney, Eds. London, U.K.: Ubiquity Press, 2017, pp. 37–60.
- [44] G. Boeing, "OSMnx: New methods for acquiring, constructing, analyzing, and visualizing complex street networks," *Comput. Environ. Urban Syst.*, vol. 65, pp. 126–139, 2017.



Arun Babu (Graduate Student Member, IEEE) received the B.Tech. degree in applied electronics and instrumentation engineering from the Government Engineering College, Kozhikode, India, in 2016, and the M.Tech. degree in remote sensing and geographic information system from the Indian Institute of Remote Sensing (IIRS), Indian Space Research Organization, Dehradun, India, under a joint education program with Andhra University, Visakhapatnam, India, in 2019. He is currently working toward the Dr.-Ing. (Ph.D.) degree in electrical engineering, electronics and information technology with the Friedrich-Alexander-University, Erlangen, Germany.

and information technology with the Friedrich-Alexander-University, Erlangen, Germany.

Since 2019, he has been with the Microwaves and Radar Institute, German Aerospace Center (DLR), Oberpfaffenhofen, Germany, as a Ph.D. Student. He has authored or coauthored about six peer-reviewed journal articles and ten conference papers. His research interests include the development of algorithms for road surface roughness estimation, cracks, and potholes detection using synthetic aperture radar datasets.

Mr. Babu was the recipient of the IIRS Golden Jubilee Fellowship—a fellowship awarded to the topper of each of the specializations in the post-graduate programs conducted by the Indian Institute of Remote Sensing.



Stefan V. Baumgartner (Senior Member, IEEE) received the Dipl.-Ing. (M.S.) degree (Hons.) in electrical and communication engineering from the Graz University of Technology, Graz, Austria, in 2004, and the Dr.-Ing. (Ph.D.) degree (Hons.) in electrical and communication engineering from the Karlsruhe Institute of Technology, Karlsruhe, Germany, in 2014.

Since 2004, he has been with the Microwaves and Radar Institute, German Aerospace Center (DLR), Oberpfaffenhofen, Germany, where he is working as a Scientist and a Project Manager. In several national and international projects, he was responsible for the ground moving target indication (GMTI) processor concepts, the performance analyses, as well as for the processor development and implementation. He also planned the first successful bistatic experiment between DLR's airborne radar sensor F-SAR and German's TerraSAR-X radar satellite, whose results were presented at the European Conference on Synthetic Aperture Radar in 2008. From 2012 to 2017, he was the Technical Lead of the European Space Agency project "Study of Multi-Channel Ka-Band SARs for Ground Moving Target Indication." Since 2010, he has been giving lectures on "SAR Moving Target Techniques" for the Carl-Cranz-Gesellschaft; and since 2016, he has been also a Lecturer with the Friedrich-Alexander-University, Erlangen, Germany. He has authored or coauthored about 20 peer-reviewed journal papers, 70 conference papers, and an invited book chapter on multichannel SAR for GMTI in the Academic Press Library in Signal Processing. He holds one patent in the field of SAR-GMTI. His research interests include the development of novel multichannel signal processing algorithms for road and maritime traffic monitoring applications using air and spaceborne synthetic aperture radar (SAR) systems, along-track interferometry, space-time adaptive processing, inverse SAR imaging, digital beamforming on receive, and time-frequency analysis.

Dr. Baumgartner successfully participated in the DLR Graduate Program, a DLR high-quality qualification initiative that accompanies the doctoral phase. In 2016, he was selected for the DLR Talent Management Program, a high calibre, and very individual personnel development tool which provides outstanding employees with intensive support over the course of 2 years.



Gerhard Krieger (Fellow, IEEE) received the Dipl.-Ing. (M.S.) and Dr.-Ing. (Ph.D.) (Hons.) degrees in electrical and communication engineering from the Technical University of Munich, Munich, Germany, in 1992 and 1999, respectively.

From 1992 to 1999, he was with the Ludwig Maximilians University, Munich, where he conducted multidisciplinary research on neuronal modeling and nonlinear information processing in biological and technical vision systems. Since 1999, he has been with the Microwaves and Radar Institute, German Aerospace Center, Oberpfaffenhofen, Germany, where he started as a Research Associate, developing signal processing algorithms for a novel forward-looking radar system employing digital beamforming on receive. From 2001 to 2007, he led the New SAR Missions Group, which pioneered the development of advanced bistatic and multistatic radar systems, such as TanDEM-X, as well as innovative multichannel SAR techniques and algorithms for high-resolution wide-swath SAR imaging. Since 2008, he has been the Head of the Radar Concepts Department, which hosts about 40 scientists focusing on new SAR techniques, missions, and applications. He has been a Mission Engineer with the TanDEM-X and he also made major contributions to the development of the Tandem-L mission concept, where he led the Phase-0 and Phase-A studies. Since 2019, he has been a Professor with the Friedrich-Alexander-University, Erlangen, Germany. He has authored or coauthored more than 100 peer-reviewed journal papers, nine invited book chapters, more than 400 conference papers, and more than 20 patents.

Dr. Krieger has been an Associate Editor for IEEE TRANSACTIONS ON GEOSCIENCE AND REMOTE SENSING, since 2012. In 2014, he was the Technical Program Chair for the European Conference on Synthetic Aperture Radar and a Guest Editor for IEEE JOURNAL OF SELECTED TOPICS IN APPLIED EARTH OBSERVATIONS AND REMOTE SENSING. He was the recipient of the several national and international awards, including two Best Paper Awards at the European Conference on Synthetic Aperture Radar, two Transactions Prize Paper Awards of the IEEE Geoscience and Remote Sensing Society, and the W.R.G. Baker Prize Paper Award from the IEEE Board of Directors.